DESIGN OPTIMIZATION AND MODELING OF PLASMONIC STRUCTURES

DESIGN OPTIMIZATION AND MODELING OF PLASMONIC STRUCTURES

By

Mohamed H. El Sherif, B. Sc. (Elec Eng.)

A Thesis
Submitted to the School of Graduate Studies
in Partial Fulfillment of the Requirements
for the Degree
Master of Applied Science

McMaster University

MASTER OF APPLIED SCIENCE (2012) McMASTER UNIVERSITY

(Electrical and Computer Engineering)	Hamilton, Ontario

TITLE: **Design Optimization and Modeling of Plasmonic Structures**

AUTHOR: Mohamed H. El Sherif
B. Sc. (Electrical Engineering, American University of Sharjah)

SUPERVISOR: Mohamed H. Bakr, Associate Professor,
Department of Electrical and Computer Engineering
B. Sc. (Cairo University)
M. Sc. (Cairo University)
Ph.D. (McMaster University)

NUMBER OF PAGES: cviii, 108

Abstract

This thesis relates itself with the study and realization of surface plasmon polaritons (SPPs) and their devices.

Plasmonics is the emerging field that will help technologies advance further into the nano-scale without the concern for delays or size limitations. SPPs are a more advanced field of photonics as they use metals instead of the semiconductors or insulators used in optics. They operate at frequencies in the light and near infrared spectrum, as this range produces their unique characteristics. Plasmonics possess the miniaturization of electronics and the speed of photonics. They do not suffer from both the delays in nano-electronics, and the size limitations faced in optics.

We provide a solid introduction to plasmonics, which includes their propagations, the different modes present, the confinement of the modes and losses, and the reasons for diverting towards SPPs. Moreover, some of the recent advances in plasmonics and their devices are introduced and discussed.

Nano-focusing using plasmonic devices is discussed and the theory behind it examined. Moreover, a novel technique for optimizing nano-plasmonic slit arrays is presented. The slits cause the bending of the light beam, where the beams from the different slits intersect and are focused at a point from the device. The proposed technique drastically reduces the number of optimization variables by using the phase profile in acquiring the slit widths. The method is demonstrated on slit arrays with different number of slits.

Furthermore, three-dimensional (3-D) chips are the new inclination towards a more compact and efficient system. Planar chips, on the other hand, suffer from congestion of components, which leads to a reduction in speed and efficiency. We present a novel 3-D multilayer plasmonic coupler for the realization of 3-D plasmonic circuits. The device takes advantage of the momentum match of the plasmonic slot waveguide and the input silicon waveguide, causing the wave to propagate vertically as well as horizontally with losses due to absorption in the metal. This method is illustrated and discussed in details.

Acknowledgements

The author wishes to express his sincere appreciation for Dr. M. H. Bakr for his expert guidance and supervision through the course of this work. Throughout the M.A.Sc program, Dr. Bakr provided encouragement, advice, and various ideas. Working with Dr. Bakr has been a great privilege for me and his calm and relaxed personality will be a life-long inspiration for my future endeavors. In addition, the author would like to acknowledge the opportunity given by Dr. Bakr to be involved in a fast tracked field, and to be entangled by different commercially available software.

The author offers his sincere gratitude and appreciation to his colleague Osman S. Ahmed for his expert advice, productive discussions, teachings and time throughout this work. He also acknowledges Osman's patience, tolerance in answering the unending questions, and guidance throughout the program.

Additionally, I am grateful to all my colleagues at the Computational Electromagnetics Laboratory at McMaster University for participating in stimulating team discussions. I was very lucky to have these wonderful colleagues and friends as they made my journey much more tolerable and pleasant.

Finally, thanks to my parents for their endless support, encouragement, understanding, and patience. Their motivation was a key factor in all my successes. I would also like to take this opportunity to thank my family in Egypt, whom their prayers followed me wherever I went.

Table of Contents

List of Figures

List of Tables

LIST OF ACRONYMS

SPP	Surface Plasmon Polariton
TM	Transverse Magnetic
TE	Transverse Electric
CMOS	Complementary-Metal-Oxide-Semiconductor
IMI	Insulator Metal Insulator
MIM	Metal Insulator Metal
PSW	Plasmonic Slot Waveguide
TLM	Transmission-line Method
FDTD	Finite-difference Time-domain
3-D	Three-dimensional
2-D	Two-dimensional
PML	Perfectly Matched Layer
IC	Integrated Circuit
FWHM	Full Wave at Half Maximum
DFO	Derivative Free Optimization

LIST OF SYMBOLS

λ_0	Wavelength in Vacuum
λ_{spp}	Surface Plasmon Polariton Wavelength
λ	Wavelength
k_x	Wave vector/Momentum/Phase constant in x-direction
k_y	Wave vector/Momentum/Phase constant in y-direction
k_z	Wave vector/Momentum/Phase constant in z-direction
k_{spp}	SPP Wave vector/Momentum/Phase constant
k_0	Vacuum Propagation constant
β	Effective Propagation Constant
ω	Frequency
ω_p	Bulk Plasmon Frequency
ω_{sp}	Characteristic Surface Plasmon Frequency
ε_m	Dielectric Permittivity of Metal
ε_d	Dielectric Permittivity of Dielectric Medium
d_x	Mode Size in x-direction
d_y	Mode Size in y-direction

c	Speed of light
w	Slit Width
d	Metal Thickness
$\square_c$	Phase constant at Center of Slit Array
$\square_{ref}$	Phase constant at Edge of Slit Array
E_x	Electric Field in *x*-direction
E_y	Electric Field in *y*-direction
E_z	Electric Field in *z*-direction
H_x	Magnetic Field in *x*-direction
H_y	Magnetic Field in *y*-direction
H_z	Magnetic Field in *z*-direction
D	Electric Displacement
P	Macroscopic Polarization

Chapter 1

Introduction

1.1 The drawback of electronic interconnects

It is undeniable that the demand for faster processing and information transport is endless. Our unrelenting need for faster, smaller, and more efficient devices has driven electronics towards the nano-scale. Now it is standard to produce ultra-fast transistors in the nano-scale range, and an illustrious example of that is the Intel microprocessor [1], [2]. Interconnects are a major component of integrated circuits (ICs) because they distribute signals, power, and clock to the various components on the IC. As the size of the components is scaled down, the performance of the circuit becomes highly dependent on interconnects. However, unlike transistors, where functionality improves with diminishing size, interconnect efficiency reduces, thus limiting the speed of digital circuits and electronic devices. As the copper interconnects are scaled down, delays increase due to an increase in the effective resistance, capacitance, cross talk, and radiation [1]-[3]. Furthermore, the time constant, which is the product of the resistance and capacitance of the line, affects the interconnect line [4]. It is evident from the resistance and capacitance equations given in (1.1) [4] that as the size of the conductor decreases its resistance increases.

$$R = \frac{\rho L}{WT}$$
$$C = \frac{\varepsilon_0 \varepsilon_r l w}{d} \quad . \tag{1.1}$$

Here, ρ is the electrical resistivity, ε_0 and ε_r are the permittivities of free space and the dielectric material, respectively. L and l are the length of the conductor and plate, respectively. W and w are the width of the conductor and plate, respectively. T and d are the thickness of the conductor and distance between the plates, respectively. It is shown that when an interconnect is scaled down to the nano-scale, R increases due to its inverse proportionality relation with W, and C increases due to the decrease in d. Moreover, copper interconnects are limited by their bandwidth and capacity, thus placing a constraint on how many components that can be placed on a chip.

Instead of using a chip with a processing core, a chip with multiple processing cores was introduced to increase the performance [5]. However, as these chips are scaled down and the number of cores is increased, the wires connecting these cores complicate the connection since they occupy a large area of the chip. Moreover, a large fraction of power gets dissipated in the connecting wires, leading to deficiencies. This happens, especially, in low power devices. As a result, this places a limit on how far cores are positioned.

An alternative would be using dielectric photonic interconnects due to their compatibility with CMOS electronics [5], [6]. The photonic interconnects offer various solutions to problems pointed out in electronics. These interconnects serve as high bandwidth and low loss interconnects between optics and electronics [6], leading to a better processing of distributed components and cores.

1.2 Silicon Photonics as the alternative key

Photonics is the science that combines optics and electronics, and involves the generation, emission, transmission, modulation, amplification, detection, and all forms of manipulating light. Dielectric optical interconnects, compared to electronic interconnects, offer increased speed and bandwidth at minimum power consumption. However, this comes at a cost of 1000 times larger optical interconnects than their electronic counterpart. Large optical devices have stimulated the need of sub-micron and nano-scale miniaturized devices in order to take advantage of their high capacity. One would want to connect the ultra-fast electronic computing units with high speed links. Ubiquitous miniaturized optical devices and interconnects are proposed owing to their ability to carry 1000 times the capacity of electronic circuits [1]-[8]. Optical networks represent the foundation for large scale digital signal communication. The scalability of these networks revolutionized the next generation integrated-on-chip optical communications.

The advances in modern day technology and the enhancement of fabrication techniques simplified the realization of optical devices. A number of silicon-on-insulator devices (SOI) have been proposed for high density photonics integrated circuits. This is partly due to their high refractive index contrast and for its excellent optical properties at optic fiber communication frequencies. In addition, silicon photonics are easily integrated in three-dimension (3-D) with other silicon based devices [5]. In [6], a Mach-Zehnder electro-optic modulator is designed and fabricated to convert the electrical signal to an optical signal. This is accomplished by encoding an optical wave with a high speed electronic signal. It is demonstrated that optical modulation rates up to 10 Gbps are obtained with low power consumption. A grating coupler using the conventional SOI has been proposed in [9]. This device promises a coupling loss below 1 dB, and ease of integration in photonic circuits. Another device, the ring resonator filter using photonic wires [10], was tested experimentally and fabricated. It had a 1 dB pass band of 310 GHz, and is CMOS compatible. Moreover, in [11] a resonant coupling type polarization splitter is demonstrated. It uses photonic crystals utilizing the photonic band-gap effect and micro-cavities. It is not easy to design a waveguide using photonic crystals due to their reduced size and high index contrast. Moreover, these crystals incur high losses compared to photonic wires [12].

Signal interconnects represent the dominant challenge that limits the speed of the digital system. Nevertheless, the size mismatch between nano-scale electronic circuits and the optical devices has limited electronic and optical integration [3], [7]. When the dimensions of optical components become close to half the wavelength of light, optical diffraction occurs restraining the propagation of light, and limiting the scalability of the optical devices [1], [3], [7]. This is due to the 3-D nature of waves propagating in a dielectric material, and is derived from (1.2) [13].

$$\beta^2 + k_x^2 + k_y^2 = \varepsilon_c \frac{\omega^2}{c^2} . \tag{1.2}$$

For a 3-D wave propagating in a dielectric waveguide with dielectric constant $\varepsilon_c > 0$, propagation constant $\beta = k_z$, and frequency ω, both the transverse phase constants k_x and k_y are real. This produces an upper limit on k_x and k_y such that $k_x, k_y \le (\omega / c\sqrt{\varepsilon_c}) = (2\pi n_c / \lambda_0)$, where n_c and λ_0 are the core refractive index and wavelength in vacuum, respectively. Due to this upper limit, a lower limit is created on the lateral mode size of the propagating wave

[13], [14] $d_x, d_y \geq (\lambda_0/2n_c)$. This makes the dielectric photonic components one or two orders of magnitude larger than their electronic counterparts. Moreover, photonic devices are frequency dependent and have a narrow bandwidth, depending on the device configuration, limiting their usage and efficiency. If the technology of the terahertz photonic components is linked with the nano-scale electronics, and high speed transistors are exploited fully, the circuit will no longer suffer from the pointed out limitations. The ultimate solution would be a circuit at the nano-scale that bridges the mismatch between the two technologies, carry optical and electrical signals, hence improving efficiency and cutting down on the chip's power consumption.

Surface plasmon polaritons (SPPs) are the answer to this problem. Plasmonics possess the high data rate capability offered by optics. They operate at frequencies in the light and near infrared regions, thus giving them the high capacity endured by optics. Moreover, plasmonics enjoy the miniaturization characteristics offered by electronics. Plasmonics use metals, including copper and aluminum, in their configurations. This feature is also demonstrated by electronics and CMOS devices as they use copper and aluminum.

1.3 Thesis Objectives

Various plasmonic structures, implemented based on different guiding and confinement techniques, have been proposed for different applications. These structures are proposed to help in the realization of integrated optics, efficient photovoltaics, nano-sensors, and high resolution focusing. The highlighted applications are important for achieving faster and more efficient technologies in the nano-scale.

The objective of this thesis is to present an efficient technique that is useful for the optimization of nano-plasmonic slit arrays. These arrays are used for nano-focusing and beam shaping. This optimization technique reduces the optimizable parameters considerably, thus saving time, computations, and memory. Moreover, this thesis proposes a novel device for the realization of 3-D plasmonic chips. The device assists in having high density integrated optics on stacked chips, as well as increasing the efficiency and computations of the system. This structure allows us to couple light from an input waveguide to different stacked layers by taking advantage of the polarization dependent nature of plasmonic slot waveguides.

The proposed technique and device aid in the advancement of optimization techniques and technology. Also, more applications are realized, especially in sensing, multilayer coupling, waveguiding, and polarization splitting.

1.4 Thesis Outline

Chapter 2 of this thesis gives a theoretical background regarding SPPs and their confinement and guiding beyond the diffraction limit of light. Furthermore, different plasmonic waveguide designs for coupling between SPPs and silicon photonics in the literature are also discussed. Additionally, a brief discussion about the use of SPPs in nano-sensors and photovoltaics are underlined. Chapter 3 illustrates our work in the optimization of the nano-plasmonic slit array, as well as the demonstration of the approach on different slit array examples. Chapter 4 is devoted to propose our 3-D coupler and polarization splitter. In this chapter, the theory behind the work, simulations using the finite-difference time-domain (FDTD) technique and the use of different materials for the coupling procedure are presented. Finally, we conclude in chapter 5 with future steps and the potential for the work discussed.

Chapter 2

SURFACE PLASMON POLARITIONS

2.1 Introduction

In this chapter, we will talk about the theory and characteristics behind plasmonics. Furthermore, some of the various applications of plasmonics are highlighted in this chapter. Moreover, several structures and devices used in different applications are discussed.

Section 2.2 will give a detailed discussion regarding the theory behind SPPs. Section 2.3 talks about the use of SPPs in waveguiding and coupling. Section 2.4 explores the use of plasmonics in photovoltaics. Section 2.5 demonstrates the use of plasmonics in optical nano-sensors. Finally, section 2.6 concludes the chapter.

2.2 Surface Plasmonics the ultimate solution

Sub-wavelength optical devices have been proposed to bridge the gap between the electronic and optical dimensions. A category of devices that are miniaturized below the diffraction limit are surface plasmon polariton (SPP) devices [1], [3]-[8], [13]. Plasmonic chips compose of optical inputs and outputs that are connected to the conventional silicon photonic devices via plasmonic couplers. In order to realize these devices, either one or both the phase constants k_x and k_y need to be imaginary [13], implying $\mathrm{Re}[\varepsilon_c] < 0$. Metals, with frequencies up to the ultraviolet, are the ideal candidates for obtaining a core dielectric index $\mathrm{Re}[\varepsilon_c] < 0$. Thus breaking the limit proposed on the lateral mode size. This aids in the realization of waveguides and cavities with effective mode areas below the diffraction limit. However, small mode size means substantial infringement of the electromagnetic wave into the metal, leading to higher attenuations [13].

SPPs are electromagnetic waves that transpire at a metal/dielectric interface, and are bounded to the metallic surface [1], [3]-[8]. They utilize the unique optical characteristics of nano-scale metallic structures to carry both electronic and optical signals. The idea of plasmonic circuits helps us combine the benefits of photonics and electronics on the same nano-scale chip. They are proposed for optical interconnects to replace the copper interconnects. Active SPP structures are proposed to overcome the inherent losses in the plasmonic circuit. The fabrication and integration for these plasmonic devices are compatible with the most advanced CMOS technology. This leads to the new era of integrated optical and electronic devices with spectacular characteristics. The routing and data transfer are done using optical interconnects without affecting the functionality of the electronic circuit [3]-[8].

The interaction of light with nano-metallic structures drove photonics into a new branch named plasmonics. Plasmonics are paving the way to the realization of sub-wavelength photonic setups for guiding and localizing electromagnetic energy for a variety of applications. This includes imaging [8], [13], nano-sensors [15], coupling [8], [13], and even photovoltaic devices for solar cells [16]. The advances in nano-fabrication and design backed the progression of plasmonics. Plasmonics carry the same capacity as the conventional dielectric photonics, and have the miniaturization feature as electronics. This circuit would first convert light into SPP waves, which propagates, processed by logic elements, and then converted to light again. SPPs have been known for decades, but it was when scientists realized that SPPs in metallic nano-structures are localized and guided beyond the diffraction limit that gave plasmonics their undeniable importance. The light waves are coupled to the conduction electrons near the surface of the metal, where the electrons collectively oscillate in resonance with the light wave giving rise to SPPs [1], [3]-[8], [13] (Fig. 2.1).

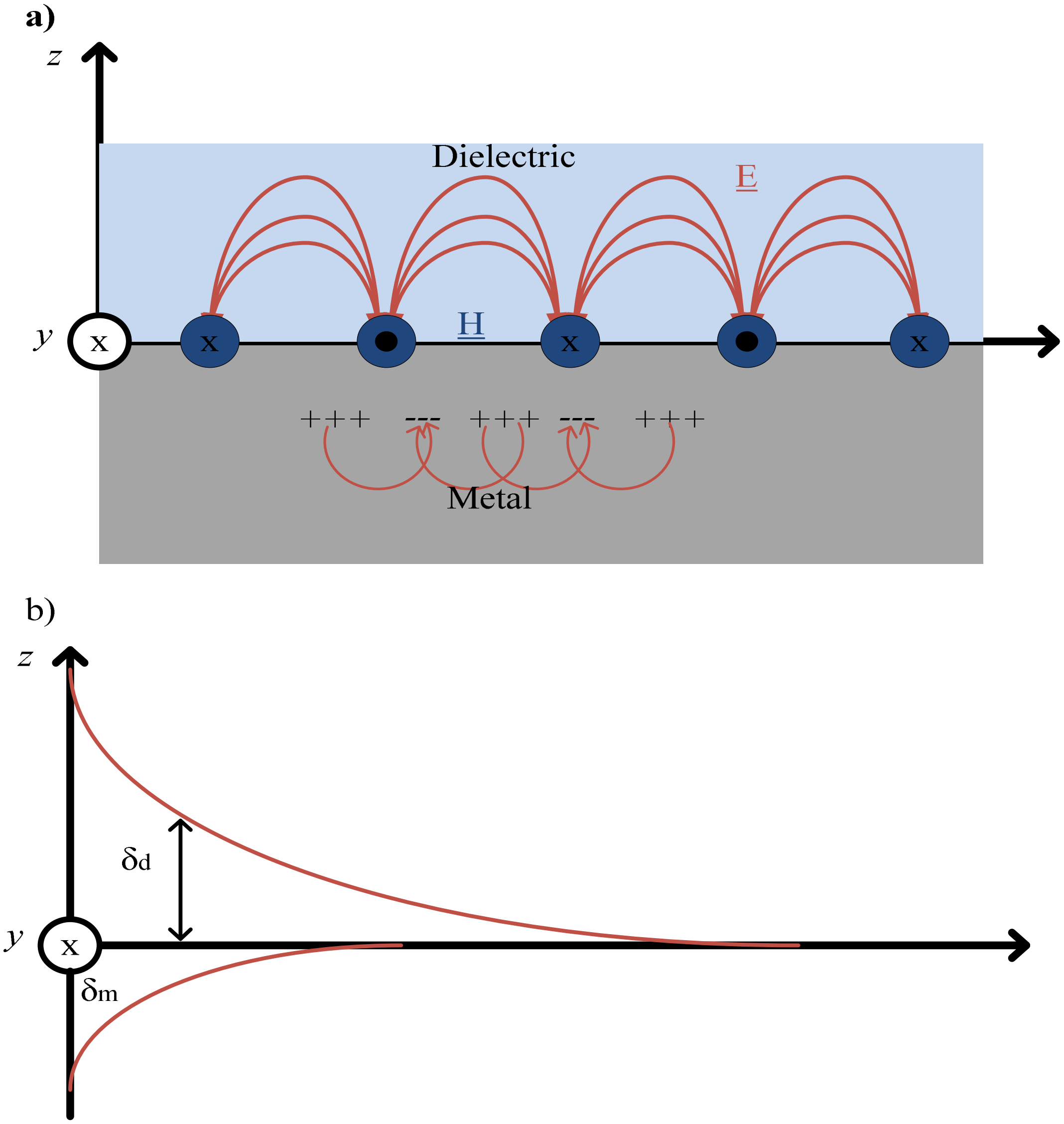

Figure 2.1 a) Electric and Magnetic fields orientations for SPPs b) Exponential decay of SPPs in the respective media.

To acquire the ability to localize and channel light in sub-wavelength metallic structures, it is important to take into consideration the different permittivities of the metal and surrounding dielectric media. The presence of metals having a negative permittivity, in a dielectric medium with a positive permittivity is a simple way in bypassing the diffraction limit, and localizing the electromagnetic wave to the nano-scale regions [1], [7]-[8], [13]. The continuity of the displacement field in the normal direction requires bound electromagnetic surface waves (Fig. 2.1). For metals, the situation where the permittivity is negative is achieved for frequencies below the bulk plasmon frequency ω_p [17].

The optical properties of metals are determined by the conduction electrons that move freely within the bulk of material, and interband excitations that occur if the energy of the photons exceeds the band gap energy of the respective metal. The existence of an electric field displaces an electron by x. The displacement is accompanied with a dipole moment μ given by $\mu = ex$, where e is the charge of the electron. The collective effect of all individual dipole moments of all the free electrons, results in a macroscopic polarization per unit volume $P = -n\mu$ [17], where n is the number of electrons per unit volume. The electric displacement $\boldsymbol{D}$ is linked to the electric field $\boldsymbol{E}$ and macroscopic polarization $\boldsymbol{P}$ by (2.1) and (2.2) respectively [17].

$$D = \varepsilon_0 \varepsilon E \quad (2.1)$$

$$D(x,t) = \varepsilon_0 E(x,t) + P(x,t) \quad (2.2)$$

Considering the motion equation for free-electron gas in (2.3), the effects of the free electrons are determined when subjected to an external electric field.

$$m\frac{\partial^2 x}{\partial t^2} + m\gamma\frac{\partial x}{\partial t} = eE_0 e^{-i\omega t} \quad (2.3)$$

Where m is the effective mass of the free electrons, and E_0 and ω are the amplitude and the frequency of the applied electric field, respectively. The equation of motion contains no restoring force since free electrons are considered. The damping term is proportional to the collision frequency $\gamma = v_F / l$, where v_F is the Fermi velocity and l is the electrons mean free path [17]. The electrons mean free path is the average distance travelled by a moving particle between successive impacts. The collision frequency corresponds to 100 THz at room temperature.

A solution of the motion equation describing the oscillations of the electrons is given by (2.4). The complex amplitude $\boldsymbol{x_0}$ contains any phase shifts between the external field and the response through (2.5).

$$x(t) = x_0 e^{-i\omega t} \,. \tag{2.4}$$

$$x(t) = \frac{e}{m(\omega^2 + i\gamma\omega)} \mathrm{E}(t) \,. \tag{2.5}$$

The displaced electrons contribute to the macroscopic polarization ***P***=-*nex*, and ***P*** becomes (2.6). By substituting (2.6) in (2.2), we get another equation relating the electric flux ***D*** with ***E***. Using (2.7) and (2.1) the simple Drude model calculating the complex permittivity is obtained in (2.8).

$$\mathrm{P} = -\frac{ne^2}{m(\omega^2 + i\gamma\omega)} \mathrm{E} \,. \tag{2.6}$$

$$D = \varepsilon_0 \left(1 - \frac{\omega_p^2}{\omega^2 + i\gamma\omega}\right) \mathrm{E} \,. \tag{2.7}$$

$$\varepsilon(\omega) = 1 - \frac{\omega_p^2}{\omega^2 + i\gamma\omega} \,. \tag{2.8}$$

Here, $\omega_p = \sqrt{ne^2/m\varepsilon_0}$ is the volume plasma frequency. According to the simple Drude model, the free electrons oscillate 180^{o} out of phase relative to the driving electric field for frequencies approaching the characteristic collision frequency of the metal, γ. This is the basic physics behind this strong frequency dependence of the optical response. As a consequence, most metals possess a negative dielectric constant at optical frequencies.

However, the Drude model needs to be improved to account for the bound electrons in the visible and ultraviolet spectrums. Thus an offset ε_∞ is added to account for the effects of higher interband transitions [17].

Metals such as Al, Cu, Au and Ag, have their plasma frequencies, ω_p, on the order of $2*10^{16}$ Hz. The plasma frequency is above light and telecom frequencies. For frequencies $\omega < \omega_p$, the metals retain their metallic character. For large frequencies close to ω_p, the product $\omega\tau >> 1$, where $\tau = 1/\gamma$ is the relaxation time. This leads to negligible damping. Here, $\varepsilon(\omega)$ is mainly real, and $\varepsilon(\omega) = 1 - \omega_p^2/\omega^2$ can be taken as the dielectric function of the un-damped free electron plasma [17].

Excitations of SPPs occur at the characteristic surface plasmon frequency $\omega_{spp} = \omega_p \big/ \sqrt{1+\varepsilon_d}$, where ε_d is the dielectric constant of the adjacent dielectric material [17]. The depolarizing effect causes the group velocity to be close to 0.

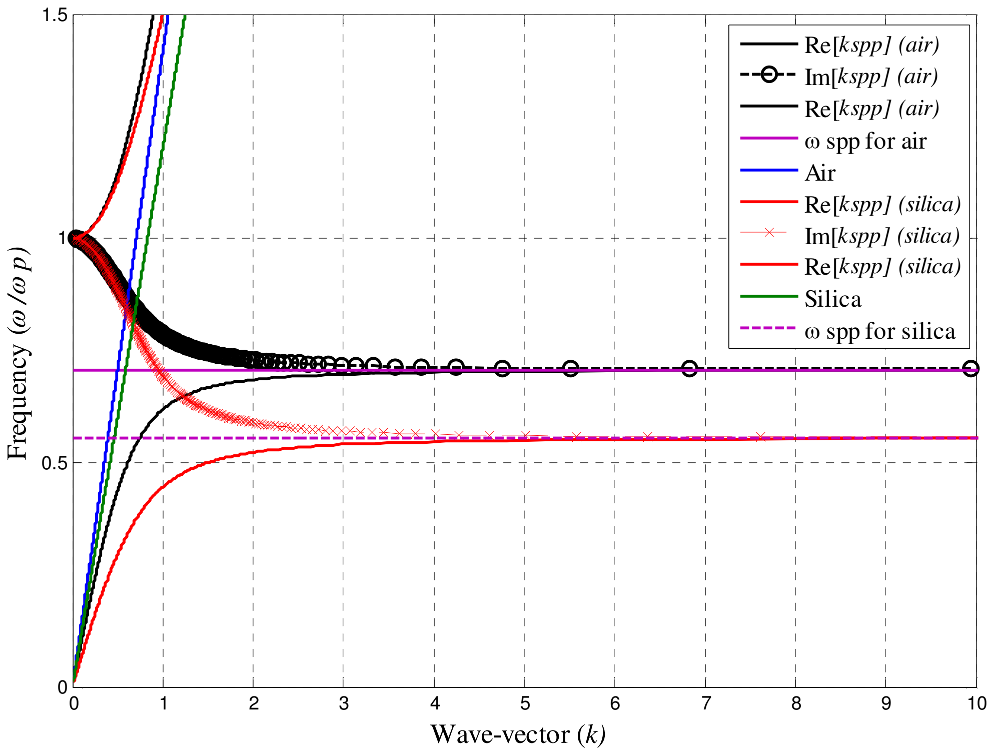

Figure 2.2 Dispersion relation for SPPs on a single interface for a lossless metal.

Figure 2.2 shows the dispersion relation of SPPs at a single metal/dielectric interface, where the dielectric constant for lossless metals is determined by the Drude model ($\varepsilon_m = 1-\omega_p^2/\omega^2$), and the dielectric materials are air and silica. There are two consequences of the interaction between the surface charges, and the electromagnetic field that make up the SPPs. Firstly, this interaction leads to a higher momentum of the SPPs as compared to that of light at the same frequency. The SPP dispersion relation is given in (2.9) [8], for the frequency dependent SPP wave vector k_{spp}.

$$k_{spp} = k_0 \sqrt{\frac{\varepsilon_d \varepsilon_m}{\varepsilon_m + \varepsilon_d}} \quad . \tag{2.9}$$

ε_m is the dielectric constant of the metal, ε_d is the dielectric constant of the dielectric material, and k_0 is the free space wave vector. The SPP excitation is on the right of the air and silica lines due to their bound character. This mismatch must be fixed to generate SPPs. Techniques for bridging the momentum mismatch have been proposed, and the main three are prism coupling, scattering from a sub-wavelength hole, and periodic gratings in the metal's surface [8], [17]. At low frequencies the SPP dispersion is close to the air and silica lines, and the waves follow a grazing incidence light field. For high wave vectors, the frequency approaches the surface plasmon frequency $\omega_{spp} = \omega_p \big/ \sqrt{1+\varepsilon_d}$, and $k_{spp} \to \infty$. Moreover, for single interface, no SPP modes exist for TE polarization [17].

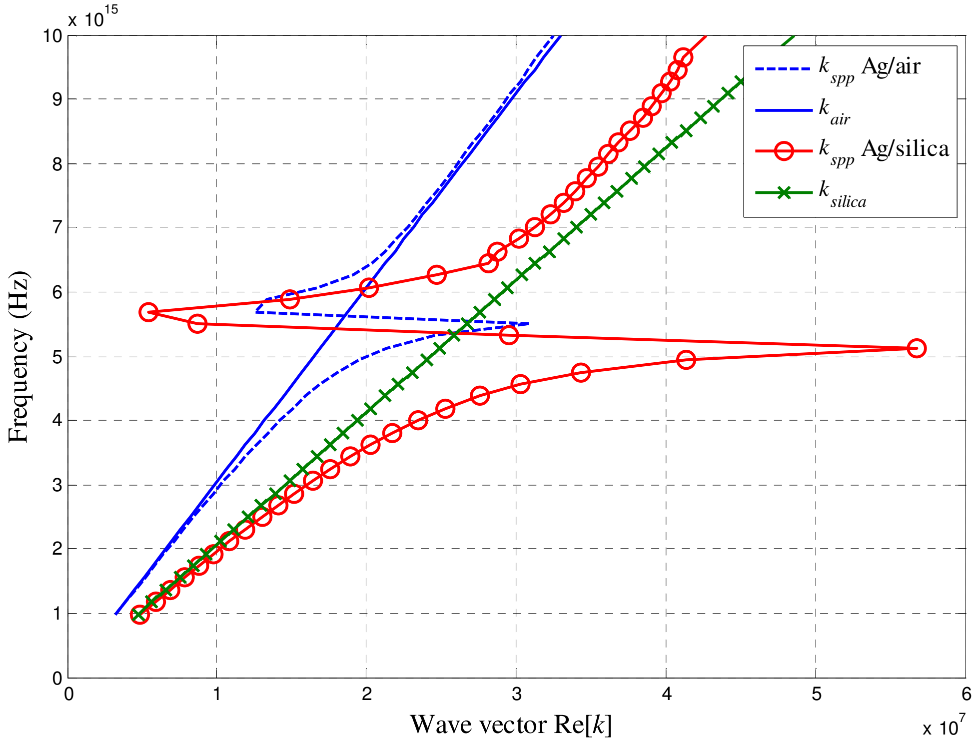

Figure 2.3 Dispersion relation for SPPs on a single interface for a lossy metal.

Figure 2.3 displays the dispersion characteristics of SPPs using the complex dielectric permittivity of the silver metal obtained from [18]. This resembles the dispersion of real metals that possess free electrons. Here, SPPs approach a finite wave vector at ω_{spp}, putting a lower bound on the wavelength ($\lambda_{spp} = 2\pi / \mathrm{Re}[k_{spp}]$) and mode confinement of the SPP (since the fields in the dielectric decay as: $e^{-|k_z||z|}, where\ k_z = \sqrt{\varepsilon_d (\omega/c)^2 - k_{spp}{}^2}$, z is the perpendicular direction to the interface). From both curves we notice that SPPs demonstrate large field confinements close to ω_{spp}. However, the field confinement is accompanied by higher losses leading to smaller propagation lengths.

The second effect of the interaction of the surface charges with the electromagnetic field is an exponentially decaying field perpendicular to the surface [8]. SPPs decay exponentially in both media, where the decay is determined by the skin depth and is usually 20-30 nm [1], [8], [13]. This displays the ability of SPPs to prevent power from dissipating away from the surface. When SPPs propagate, their power gradually attenuates owing to the resistive losses, absorption in the metal, and coupling from radiation [1], [8]. The most commonly used metals for guiding SPPs are silver and gold because they exhibit the lowest losses in the visible spectrum [8]. It was due to this absorption in the metal that SPPs were not considered practical for guiding and propagating. Now, plasmonics are being considered as a major component in integrated circuits.

The guiding of SPPs is a vital topic of research. Plasmonic waveguides are an essential component for realizing plasmonic chips, as well as coupling to photonic or even electronic devices. A variety of techniques for guiding SPPs have been proposed, however, metal-insulator-metal (MIM) and insulator-metal-insulator (IMI) waveguides are extensively researched [17], [19]. IMI, as the name implies, is formed by placing a thin metallic film (< 50 nm) between two dielectric materials of the same or different refractive indices. This resembles a combination of two dielectric/metal interfaces, where the exponentially decaying field, inside the metal, from one interface couples to the other. This results in the guiding of two leaky waves [13], [19]. The IMI guiding scheme offers long propagation lengths of multi-centimeters. IMI structures include metal films or stripes, which are used to guide long-range SPPs (LRSPP). The propagation distance is in tens of microns or even millimeters. However, decreasing the thickness of the strip or its width, results in worsened localization of the mode [7], and a shortened propagation length [3], respectively. On the other hand, short-range SPPs (SRSPPs) have higher localization but shorter propagation distances, and are better suited for integrated circuits [7]. In [20] a coupling technique, with 80% coupling efficiency, between plasmonic and photonic nano-wires has been proposed. Furthermore, this configuration was used to realize a Mach-Zehnder interferometer, a polarization splitter, and micro-ring cavities. Even though the confinement is subwavelength, the propagation length is very small. Moreover, in IMI structures, the mode confinement is not always sub-wavelength due to the wave's weak normal confinement. The field has a long decay length in the surrounding dielectric, and it is difficult to integrate on a chip due to radiation and coupling from other devices [13], [19]. The dispersion relation for the IMI structure is given by (2.10) [17].

$$\tanh(k_1 a) = -\frac{k_2\varepsilon_1}{k_1\varepsilon_2}$$

$$\tanh(k_1 a) = -\frac{k_1\varepsilon_2}{k_2\varepsilon_1}. \tag{2.10}$$

Where $k_i^2 = \beta^2 - k_0^2\varepsilon_i$ is the wave-vector in the respective medium, ε_i is the permittivity in the respective medium ($i = 1, 2$). Figure 2.4 shows the leaky and bound modes in the IMI configuration. Figure 2.5 illustrates the odd ($E_x(z)$ is odd, $H_y(z)$ and $E_z(z)$ are even functions) and even ($E_x(z)$ is even, $H_y(z)$ and $E_z(z)$ are odd functions) parity vector equations for the dispersion relations in an IMI structure. The metal slab thickness is 50 nm and 100 nm. As the metal film thickness is decreased, the confinement of the odd modes to the metal decreases [17]. This results in an increased SPP propagation length because the mode changes to a plane wave supported by the dielectric medium. However, the even modes' confinement increases with decreasing the thickness of the metal, leading to small propagation lengths.

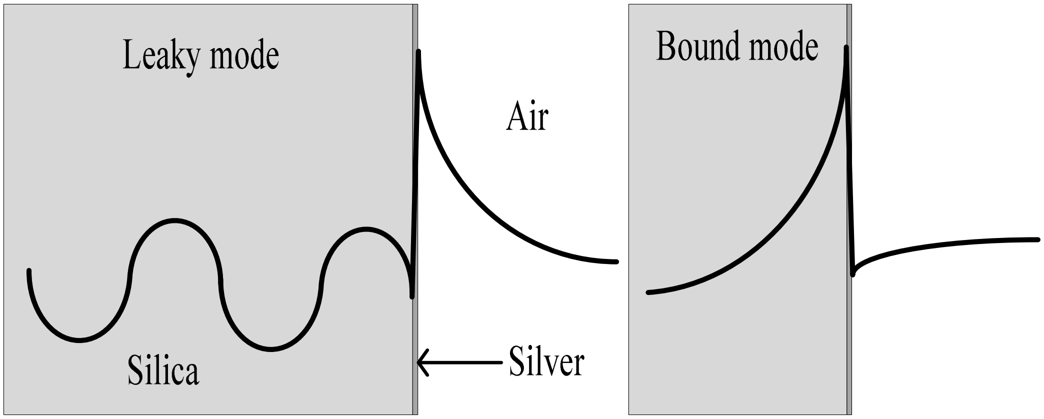

Figure 2.4 Leaky and bound modes for IMI structures.

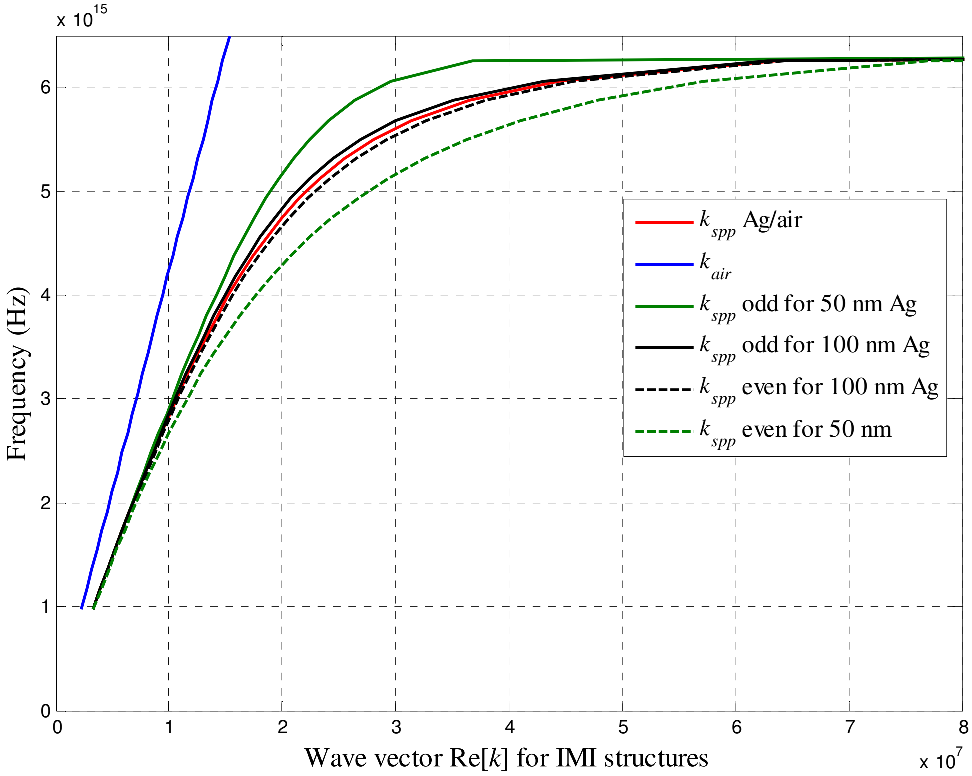

Figure 2.5 Dispersion relation for IMI structures.

The second configuration that allows subwavelength confinement and integration is the MIM geometry. Figure 2.7 displays the dispersion curve for the MIM geometry. As the gap is reduced, the propagation constant increases, implying a more confined mode. Although this structure has short propagation lengths compared to IMI, it has strong mode confinement, easily integrated in photonic chips, and is not affected by radiation or cross talk [17], [19]. The dispersion relation for MIM structures is given by the first equation in (2.10), as this resembles the odd parity vector equation. Figures 2.6-2.7 show the mode present in the MIM structure, as well as the wave vector for this structure with air as the dielectric slot. It is seen that MIM obtain large wave vectors by adjusting the dielectric core width, and thus reducing the penetration in the metal. This demonstrates that MIM structures can sustain localization effects even in the infrared.

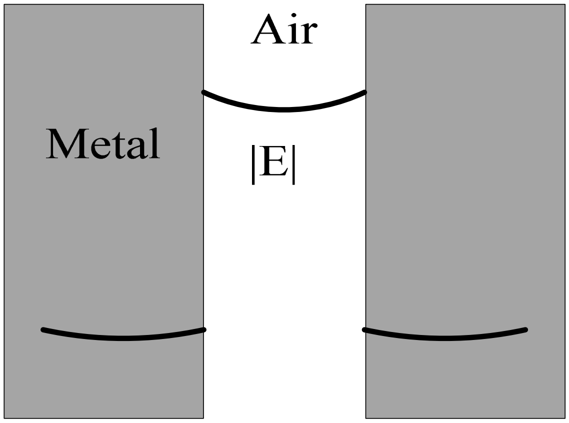

Figure 2.6 Mode in MIM structures

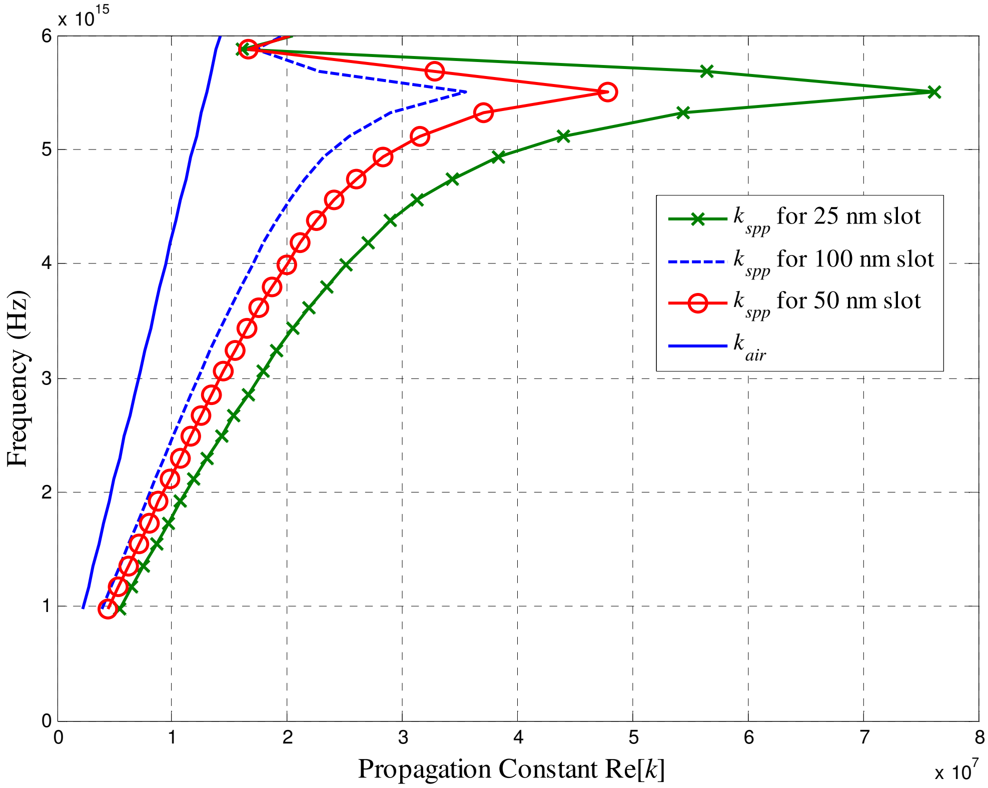

Figure 2.7 Dispersion relation for MIM structures

Plasmonics are thus paving way to the realization of more compact and efficient systems. However, the mode mismatch between both plasmonics and silicon photonics presents a prime challenge. Plasmonic coupling has been extensively researched, producing promising structures and devices. The waveguides implemented using IMI [21], MIM [22], and hybrid waveguides [23], are used in the different coupling approaches. They are potential candidates for the coupling scheme. Each of the proposed plasmonic guiding waveguides has its advantages and disadvantages depending on the application. The problems range from difficulties in fabrication, higher dissipation losses, poor localization, sensitivity to structural deficiencies, and integration with current technology [1], [3]-[8].

2.3 Surface Plasmons in waveguiding and coupling

The orthogonal coupling technique using plasmonic slot waveguides (PSW) [24], which is a 3-D variation of the MIM where a subwavelength slot is placed between two metals in the horizontal direction and dielectric in the vertical directions, demonstrated a coupling efficiency of ~70%. PSWs allow only one mode to propagate (TM), while completely reflecting the other mode (TE) [25].This method uses the idea of wave vector matching to improve the guiding. By matching the dielectric wave vector from the silicon waveguide to that of the PSW, the wave is coupled efficiently from the silicon to the plasmonic waveguide. The coupling procedure is demonstrated experimentally and showed promising results. Figure 2.8 shows the proposed structure.

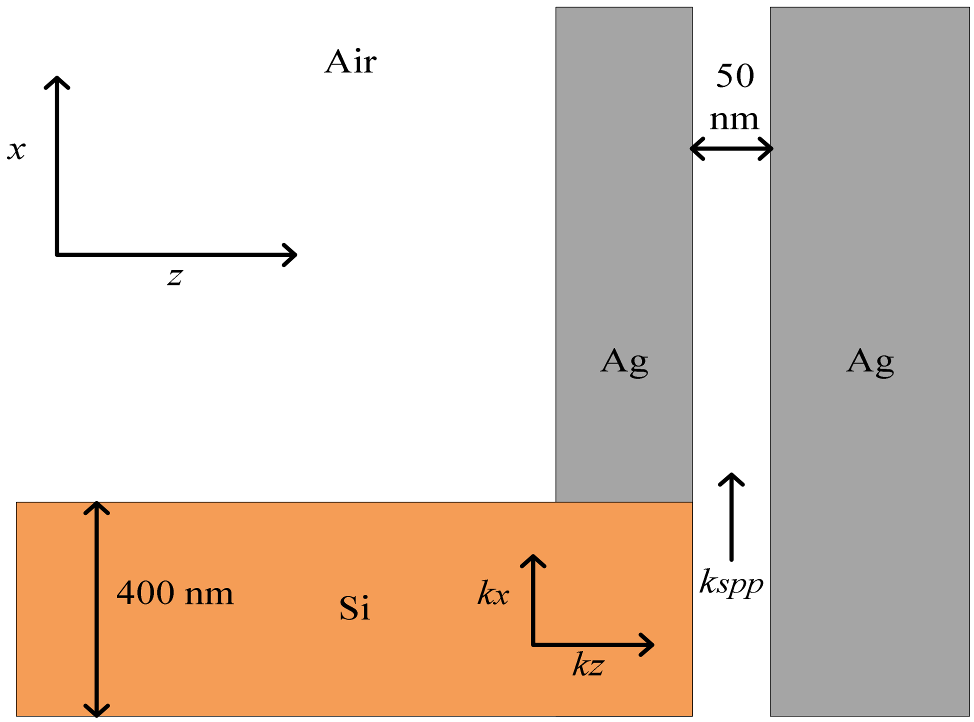

Figure 2.8 Proposed orthogonal coupling structure.

Another coupling technique is demonstrated in [23], which uses a hybrid plasmonic waveguide that is composed of a metal-insulator-Si-insulator-metal configuration. This scheme uses tapers to smoothly convert the field from the dielectric waveguide into the SPP waveguide. The technique demonstrated a coupling efficiency of > 90% at 1.55 μm, and is CMOS compatible due to its use of copper or aluminum in its structure. Here, the field travels in the insulator due to its continuity when it is normal to the metal/insulator and insulator/Si interfaces. The introduction of the insulator layer in the slot of the waveguide reduces the propagation loss. Moreover, this device guides the light efficiently at sharp bends. The structure was fabricated and tested and showed strong correlation with the simulation results. Figure 2.9 displays the configuration of the device.

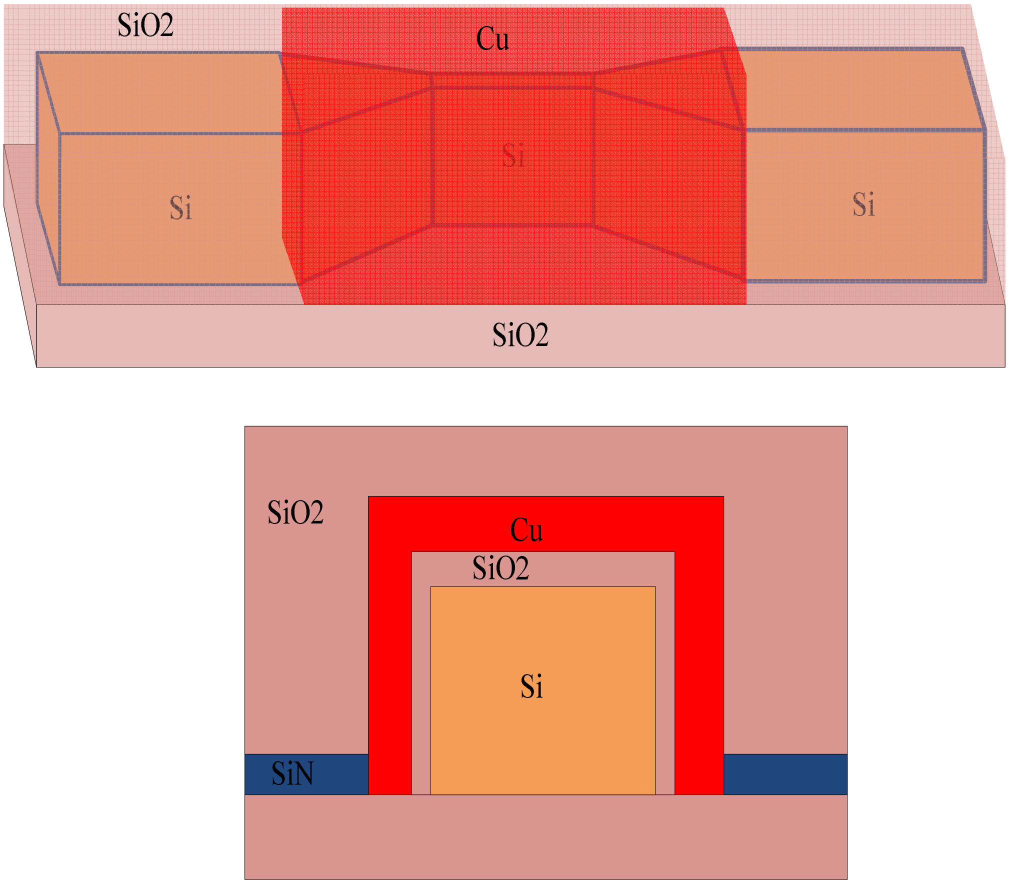

Figure 2.9   Proposed Hybrid coupler

In [26], an ultra-compact coupler and splitter is proposed. The device has a coupling efficiency of 88%, and 45% coupling efficiency for a 1 x 2 splitter. Here, an air-gap coupler (AGC) is used and its design optimized to obtain the best results. Misalignment analysis between the AGC and the silicon waveguide or MIM has been studied. The optimum configuration is by having the Si waveguide edges aligned with those of the AGC, and the MIM has to be placed at the center of the Si waveguide. Furthermore, the splitting functionality of this technique is studied, and its dependence on the AGC's width, length, and alignment examined. This coupling method is potentially used as a Mach-Zehnder interferometer or a directional coupler. The coupler/splitter device is illustrated in Fig. 2.10.

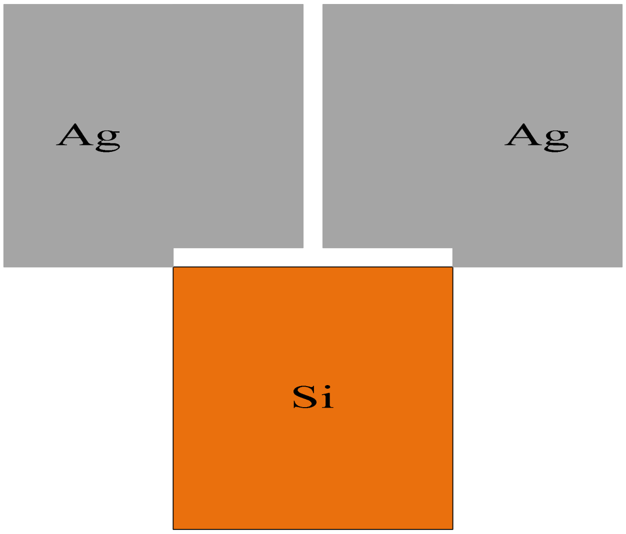

Figure 2.10 Proposed Ultra-compact coupler

A silicon based plasmonic waveguide interfaced to the silicon photonics platform is presented in [27]. This device works at telecommunication wavelengths and illustrates the potential of silicon photonics and silicon plasmonic integration. The structure consists of a SOI waveguide capped by a 50 nm thick gold layer. To fabricate the desired waveguide, two layers of electron beam lithography (EBL) were used. The first EBL defines the SOI waveguide couplers, while the second EBL defines the plasmonic features. The propagation distance and coupling efficiency were found to be 2 µm and 38%, respectively, at 1.55 µm. Moreover, the device demonstrated broadband characteristics, and its ability to be merged in CMOS circuitry.

2.4 Plasmonics in Photovoltaics

SPPs are not just interesting for waveguiding, integrated circuits, nano-focusing, or sensors; they are also of great interest in the design of photovoltaic devices. The study of photovoltaics is the conversion of sunlight to energy, and promises to allow the generation of electrical power on a large scale. Currently, photovoltaics are based on the silicon crystalline wafer, which consumes most of the cost of solar cell production. Silicon is an ideal photovoltaic material with a lot of necessary characteristics. Thin film solar cells have gained a lot of interest because of their lower fabrication costs [16]. However, a drawback is the low absorbance of near band-gap light as the thickness of the material is reduced. For increased absorbance, the thickness of the cell has to increase and this leads to higher costs. Furthermore, the conventional light trapping technique using a pyramidal surface texture causes the size of the geometry to increase. The large surface area increases minority carrier combination in the surface and junction regions. By proper design of surface plasmon nano-structures, light is concentrated and guided into the semiconductor layers, and thus increasing absorption. Solar cell design and material formation or selections are affected by optical absorption thickness versus carrier collection length. Plasmonics, on the other hand, overcame this limitation by using metallic nano-particles, or grooved metallic films, and thus simplifies the use of Si thin-films.

When a nano-particle is placed close to an interface between two dielectrics, light scatters into the dielectric with the larger permittivity [28]. The scattered light gains an angular spread in the dielectric that increases the effective optical length. Moreover, light scattered at an angle beyond the reflection angle is trapped in the cell. The size and shape of the nano-particles are important for the coupling efficiency [16]. Smaller particles, with their effective dipole moment closer to the semiconductor layer, couple a larger portion of the incident light into the semiconductor. Metal nano-particles are tuned to resonate at different frequencies by surrounding them with different dielectric materials [29], [30]. However, in nano-particles, ohmic losses increase with volume, while scattering increases with the square of the volume. It is also important to consider coupling between particles, ohmic damping, and coupling to waveguide modes.

Moreover, taking advantage of the strong local field enhancement of the nano-particles is another way for the resonant plasmon excitation on thin film solar cells. The nano-particles act as an effective antenna, storing the incident light as energy in a localized SP mode. This type of storage is useful for materials where the carrier diffusion lengths are small and where photocarriers are generated close to the collection junction [31], [32].

Another technique for trapping the light is by the confinement of the evanescent fields generated from the conversion of light to SPPs at the metal and semiconductor interface. At the resonant frequency (350 – 750 nm) these fields are confined near the interface at a dimension smaller than the wavelength. Light is absorbed along the parallel direction of the solar cell, and this technique is easily implemented in solar cells because metal is a standard element used in such devices. As is the case there is a tradeoff between propagation length and optical confinement. Furthermore, to have efficient light trapping, absorption in the semiconductor should be stronger than in the metal [16]. To match the momentum between the incident light and the SPP mode a metal ridge is used [8], [17], [33]. Furthermore, light trapping using this technique is insensitive to the angle of incidence [33]. At the present time, there is a lot of research on using metal back reflectors in solar cells for light trapping, and it is vital to carefully design the cell to account for scattering and localization [34], [35]. Moreover, plasmonic light trapping improves the electrical features of the solar cell [36], and improves the efficiency of the cell in a logarithmic fashion.

2.5 Surface Plasmons in Optical Nano-Sensors

In the previous sections, SPPs were used for guiding and light trapping, and showed different properties for different dielectrics and metals used. Thus it is evident that SPPs are sensitive to the refractive index changes around the metallic surface, which attracted a lot of attention from researchers for its prospective use in optical sensing applications. For sensors using plasmonics, two types of plasmon modes are usually used due to their sensitivity to refractive index changes when the target compound binds to the surface. These modes are propagating surface plasmon resonances (PSPRs) [37] and localized surface plasmon resonances (LSPRs) [38]. PSPRs are evanescent electromagnetic waves confined by the metal/dielectric planar interfaces, and efforts for signal enhancement by increasing the binding surface and appropriate surface configuring have been employed [37]. LSPRs are electromagnetic waves confined on the metallic nano-structures, and comprise the advantages of PSPRs, as well as its sensing abilities are tuned by changing the shape, size, and structure of the nano-particles [38]. Thus LSPRs are the center of major research in order to improve sensors [15]. Most of the work done with LSPRs is based on the combination of different signals from different particles of different sizes.

SPPs have an exponentially decaying field away from the dielectric/metal interface. Changes in the refractive index above the interface, shifts the plasmon resonance condition, which is detected as changes in intensity, wavelength, or angle shifts. This is the sensing principle used in sensing applications. SPR spectroscopy is used for the real time classification of molecular interactions on liquid/solid interfaces [39]. It comprises of the excitation of SPPs on silver or gold films using lateral-polarized waves, and reflectivity is measured as a function of the incident angle. Changes on the surface result in SPR angle shifts because SPR is very sensitive to the dielectric constant directly neighboring the metal film. SPR spectroscopy uses planar thin metallic films, and is similar to devices utilizing PSPR modes. PSPRs have been exploited to detect molecules in different fields, and its sensitivity is enhanced by carefully designing the sensing layer [39]-[41].

LSPRs, on the other hand, are confined waves that are excited on metallic periodic nano-holes [42] or arrays [43]. The magnitude and spectral position of LSPRs are dependent on the geometry of the arrays, their composition, and local dielectric environment, making it easier to optimize the nano-sensor by designing a geometry responsible for the local refractive index changes [15]. Spectral shifts are monitored in real time with high sensitivity by simply summing the absorption and scattering of the nano-structure [15]. In addition, LSPR allows the improved sensitivity of changes in the surrounding environment. They are used to detect non-resonant [44] and resonant molecules [45]. LSPRs are combined with other techniques, like surface-enhanced Raman scattering (SERS), to develop enhanced molecular identification platforms [15]. However, although LSPR periodic arrays are more sensitive than PSPR methods, challenges in fabrication and group averaging effects remain.

Using the LSPR technique with single nano-particles (S-LSPR), develops a very sensitive optical sensing platform. S-LSPR sensors have many properties like, large optical cross section, non photobleaching, high water solubility, and are easily observed by using dark filed microscopy [15]. For example, a single gold nano-particle in solutions shows a sharp symmetric resonance peak that distinguishes them from a group of gold particles, which have a broader, non-symmetric spectrum [15]. When using S-LSPRs the system has a high spectral resolution as compared with PSPR or LSPR systems. Moreover, they are sensitive to thermal-induced fluctuations of the sample than group (ensemble) mode sensors. However, they suffer from giving molecular specific information.

A technique, based on S-LSPR modes, that improves selectivity and sensitivity is plasmon resonance energy transfer (PRET). When nano-particles' resonance spectrum matches that of the molecules bounded on the nano-particle, PRET is observed by wavelength quenching or dips in the spectrum. PRET based methods allow for high selectivity as well as spectral sensitivity, since it occurs for binding specific molecules [15]. Another method, based on S-LSPRs, to monitor biomolecular distances or trajectories between nano-particles is plasmon coupling or the plasmon ruler [46]. This method studies the kinetics of DNA samples. When the DNA particles interact with metallic nano-particles, the scattering from the metallic nano-particles changes the color [15]. This change in color is caused by the formation of nano-particle pairs, which lead to a spectral shift in the wavelength. Measurements using this method are beneficial because long distances of up to 70 nm are measured for long periods of time. This method was recently employed to in vivo (living cells) works, and trajectories of living cells were monitored for two hours [47].

2.6 Conclusion

In this chapter we discussed the origins of SPPs, the theory behind their operation, and their unique features. We also talked about their characteristics for single and multilayer interfaces. Then, the discussions about different plasmonic waveguides and their uses were presented. Moreover, some light was shed on the uses of plasmonics in photovoltaics and nano-sensors, and the various works done in these areas.

Chapter 3

Nano-Focusing and Nano-Plasmonic Structures

3.1 Introduction

In the previous chapters, an introduction to plasmonics and why they are leading the way in modern day research was given. It is due to plasmonics' unique characteristics that make them potential candidates for various applications. In this chapter, we will discuss the use of plasmonics in realizing optical lenses. Plasmonic lenses use the unique features offered by SPPs to realize sub-wavelength resolution, focusing, and beam shaping.

In section 3.2, the use of plasmonics in optical lenses and achieving nano-focusing is investigated. Furthermore, various methods for achieving improved focusing are highlighted. Section 3.3 will introduce a novel method for optimizing slit array structures. This method efficiently optimizes slit array structures using the parameters of a simple parabolic profile equation. The approach and the conducted tests are all given in the section. Finally, section 3.4 that concludes this chapter will be presented.

3.2 Plasmonic lenses and Nano-focusing

As discussed earlier, optical devices are limited by the diffraction limit. This diffraction limit also places a constraint on the achieved resolution of optical lenses. To improve the resolution, one can focus the evanescent fields in the near-field region. When the permittivity and permeability of a material are both equal to -1, a perfect lens is realized [48]. However, due to dispersion and absorption in materials it is hard to satisfy this condition [49]. Plasmonic lenses, on the other hand, provide higher resolution beyond the diffraction limit for focusing, imaging, and beam shaping. They also possess extraordinary enhanced transmission characteristics [8], [49]. Superlenses [50] and hyperlenses [51] have been proposed, that show enhancement in the evanescent waves as they pass through silver films. They provide sub-diffraction-limited images of objects. The superlensing effect is achieved when the structure is excited with a transverse magnetic (TM) wave. Additionally, the dielectric constant of the metal, ε_m, and the dielectric material, ε_d, have to be equal ($|\varepsilon_m| \approx \varepsilon_d$). Superlenses do not possess working distances. Their decay length is short, have no amplification, have one-dimensional (1-D) imaging, and their fabrication is complex. However, hyperlenses can magnify the image and project it into the far field. The object is usually inscribed inside the inner surface of the cylindrical lens [49], and the object is magnified in the radial direction of the multilayered structure. Hyperlenses also suffer from no working distance, and complexity of fabrication. These lenses are difficult to consider for practical applications, but nevertheless they opened the way for plasmonic lenses.

Creating grooves or slits in a metallic layer allows the formation of a light beam with a width comparable to that of the wavelength of light. Sub-wavelength holes played a major role in nano-plasmonics after the discovery of extraordinary transmission (EOT) [8]. It displayed large peaks in the transmission spectra at wavelengths larger than the aperture size. A breakthrough came when the propagation through rectangular holes could be modeled accurately with two coupled Surface Plasmon Polaritons (SPPs) on each side of the hole, known as metal/insulator/metal waveguide mode [8]. This has the possibility of a high efficiency of SPP excitation.

1-D sub-wavelength metallic structures have been proposed for the focusing of light [52]-[54]. These structures are based on either depth tuning or width tuning to achieve the required focusing. Moreover, the number, and periods of grooves are used to alter the diffracted beams to produce sub-wavelength resolution and nano-meter accuracy. In depth tuning, the depth of each groove or slit is designed to achieve the needed focusing. The width of each groove is usually smaller than half the wavelength of the incident wave designed for high diffraction efficiency [55]. There are three depth tuning configurations, which include concave, convex, and flat groove depth [49], [52] (see Fig. 3.1). When a TM polarized wave is incident on the slits, SPPs are excited and propagate along the metallic surface where they are diffracted to the far field by the grooves. The diffracted signals from each groove interfere constructively, leading to the focusing effect on the beam axis. The focusing takes place when the phase difference between the light exiting the slit and the grooves is multiples of 2π [52]. It has been shown in [52] that the phase at the exit of each groove increases with the increase in depth, leading to an increase in phase retardation without the need to increase the number of grooves. For depth tuning, the best groove configuration for focusing is the concave structure.

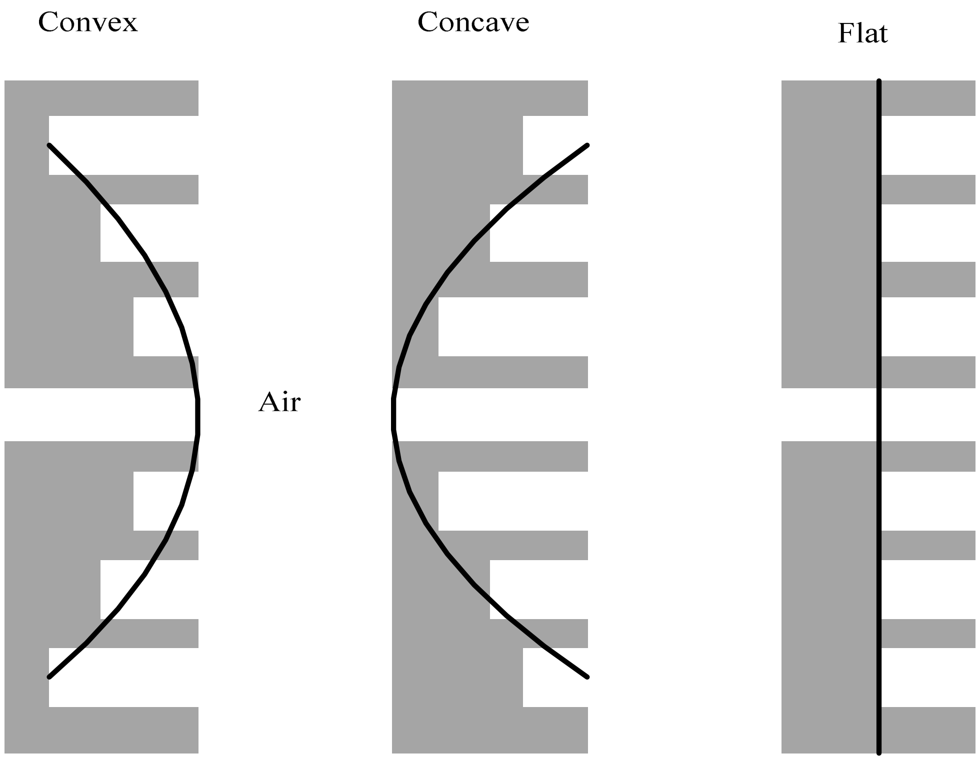

Figure 3.1 Different width tuning configurations

The second method for sub-wavelength focusing is width tuning of the grooves or slits. Various methods have been proposed to manipulate light by modulating the light phase of arrayed slits by altering the slit widths while keeping the depth constant [53], [54]. The electromagnetic energy in the nano-metric waveguides are guided as SPPs. The waves in these waveguides provide phase retardation with varying phase propagation constants for different widths. The phase modulation achieved by varying slit widths is apparent from the dispersion relation between the effective refractive index and the slit width given in given by [53]:

$$tanh(\frac{w_i\sqrt{\beta_i^2-k_0^2\varepsilon_d}}{2})=-\frac{\varepsilon_d\sqrt{\beta_i^2-k_0^2\varepsilon_m}}{\varepsilon_m\sqrt{\beta_i^2-k_0^2\varepsilon_d}}. \qquad (3.1)$$

β_i is the propagation constant of the ith slit, k_0 is the free space propagation constant, ε_m and ε_d are the permittivity of the metal and dielectric, respectively. Each nano-slit is independently controlled to produce its phase, leading to flexibility in the design of these structures [49], [53]. Fig. 3.2 demonstrates the change in the real and imaginary parts of the wave vector when changing slit widths. This method is implemented in beam shaping, data storage, integrated optics, and near-field imaging. In [53], a metallic film is designed with a number of nano-slits having different widths. The light impinging the structure from one side is modulated and converges to a point on the other side. The focused beam is observed 0.6 μm away from the structure with full wave at half maximum (FWHM) of 270 nm. This demonstrated the sub-wavelength focusing of the structure and by careful design of the slit widths, further focal points with sub-wavelength beam widths are achieved.

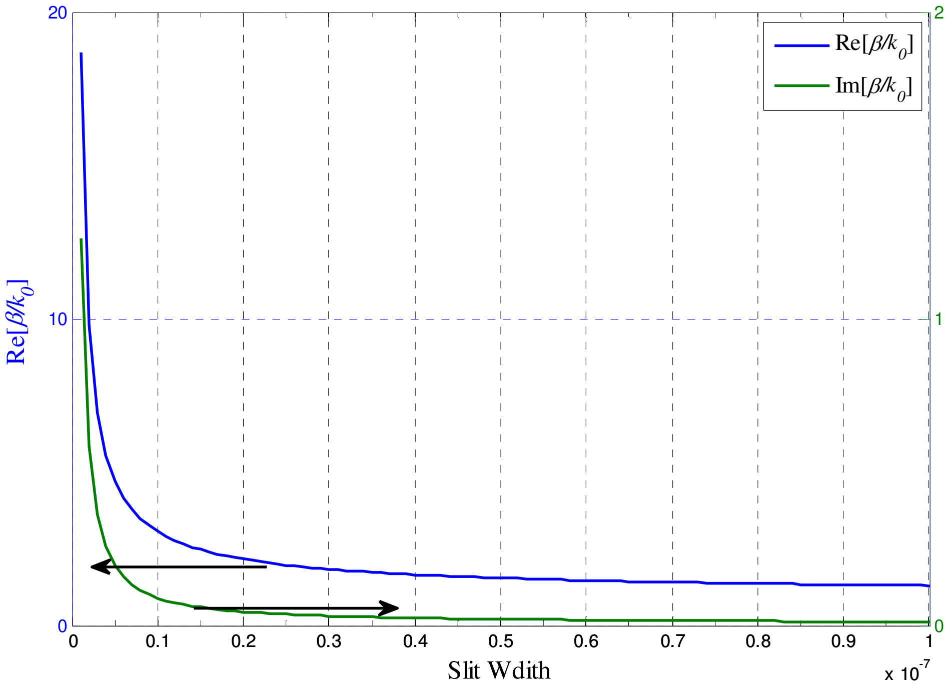

Figure 3.2 Real and Imaginary part of the wave vector with changing slit widths

Another design using the width tuning method is proposed in [54]. The work presented here, demonstrates how fabricated lens' behavior differs from that in simulations and theory. A gold metallic opaque film is used in this experiment. The spacing between the slits is larger than the skin depth to avoid coupling between the slits. A single-pass phase delay of $\beta_i d$, where d is the metal film thickness and β_i is calculated from (3.1), is introduced. Light travels slower in narrower lists, due to a large part of the mode residing in the metal. As a result, when we have slit widths increasing from the center of the array to the edges, a parabolic (curved) wave front is obtained. The focal length and beam width obtained experimentally from the designed structure are 5.3 µm and 0.88 µm, respectively. The experimental results are in good agreement with the simulation results. However, they are inconsistent with the theory. The focusing behavior is controlled by changing the lens size. The lens size is a major reason for the inconsistency between the simulations and the theory. Moreover, the phase delay is altered due to oscillations in the slits. Furthermore, the transmission of each slit varies depending on the slit width. Yet, all of these deviations are accounted for in simulations, but not in the simple theory. This results in shorter focal lengths obtained in simulations and experiments as compared to the theory. From [54], it is pointed out that the slit spacing has a minimal effect on the structure, and that lenses with short slits cannot achieve far focal points.

2-D plasmonic lenses have also been proposed by shining the incident light on planar circular gratings [49], [56], [57]. The measurements illustrate that the circular lens achieves ten times the intensity of a single ring for the in-plane components. In [56] the proposed lens produces long depth of focus (DOF) and focal length in the range from λ to 8λ, making auto-focusing easier at a working distance for optical systems. Additionally, as the thickness of the used metal is changed, the peak transmission shifts. This helps in realizing a free feedback control system for auto-focusing. Here, the probe scanning is made with a constant working distance from the probe to the sample surface. This is done provided that the flatness variation of the sample substrate is within the DOF. Another circular plasmonic lens is proposed in [57]. It displays tight focusing of the SPP waves, with a spot size of 0.38λ, when excited with a radially polarized light. The experiments demonstrated the role polarization plays in focusing, where linear polarization generates SPPs from regions where the incident polarization is TM polarized with respect to the slit. Moreover, linear polarization cannot produce a sharp focus. These lenses are used in applications such as optical memories or for sensing [49], [56], [57].

3.3 Efficient optimization of Nano-Plasmonic Slit Arrays

SPPs decay exponentially in both metal and dielectric media, where the decay is determined by the skin depth [1], [8]. This offers the ability to localize and channel light in sub-wavelength metallic structures. SPPs suffer, however, from losses due to absorption in the metal and unwanted radiation [1]. Metallic plasmonic structures have been recently proposed for sub-wavelength operations at optical frequencies [54]. Optimized designs for a desirable functionality are mandatory. However, little work has been dedicated to the optimization of these devices. Optimizing nano-plasmonic structures has always been a challenge. Accurate numerical approaches must be utilized in order to properly model all the device characteristics and parameters. In the optical range, the electrical size of structures is fairly large which requires intensive simulation time. Furthermore, as the optimization parameters increase so does the simulation time and the difficulty in optimization.

In [58], a Genetic Algorithm (GA) is proposed for the optimization of metallic slit arrays. A large number of time-consuming initial simulations are needed. Moreover, the population parameter is essential for the accuracy of the results. A similar approach is reported in [59] where a Particle Swarm Optimization (PSO) algorithm was used. Moreover, the complexity of the technique used increases with increasing slits.

Here, we propose a novel approach for the efficient design optimization of plasmonic slit array structures. Using a semi-analytic model, we reduce the optimization problem from one with many parameters to a simpler one with only two parameters. One parameter controls the required phase profile of the array, which has a parabolic behavior. The other parameter controls the phase offset in order to vary the maximum slit width at the edges of the array from 100-210 nm. A mapping is established between the physical parameters and the optimal phase profile. The width of each slit is determined by its optimal phase at the slit's position in the array. Derivative-Free Optimization (DFO) is utilized in optimizing the structure. A multi-objective formulation enables us to optimize, simultaneously, the focal length and the full wave at half maximum (FWHM) (beam width). Time-domain transmission line modeling (TLM) [60] is utilized in modeling the slit array structure. Our results are verified through Lumerical's commercial simulator FDTD Solutions [61]. In the next section, the slit array under consideration and the proposed technique are discussed. Then, we discuss the results obtained with this method, for different slit arrays, to show its operation.

3.3.1 Nano-scale Slit Array and Formulations.

A simple plasmonic structure has been recently proposed to achieve non-ordinarry effects [54]. An array of metalic slits are organized with an optimized shape (slit width) and periodicity. The structure considered in this work is shown in Fig. 3.3. It has the ability to focus light over a given frequency band by varying the slit widths [54]. Lens effect has been reported for such a struture [54], where the light is focused at sub-wavelength dimensions. The focused light is thus utilized for accurate optical microscopy and CMOS image sensors [58]. For ease of fabrication, the structure's metal thickness is taken as h = 400.0 nm [54]. The dielectric constant of SiO_2 is 2.13. The metal used is gold with a dielectric constant of −11.04 + 0.78i at a wavelength of 637.0 nm [54]. The widths of the slits are chosen to achieve a parabolic phase profile [53], [54], where the phase shift of the light at each slit depends on the thickness of the metal and velocity of propagation inside the slit as discussed before.

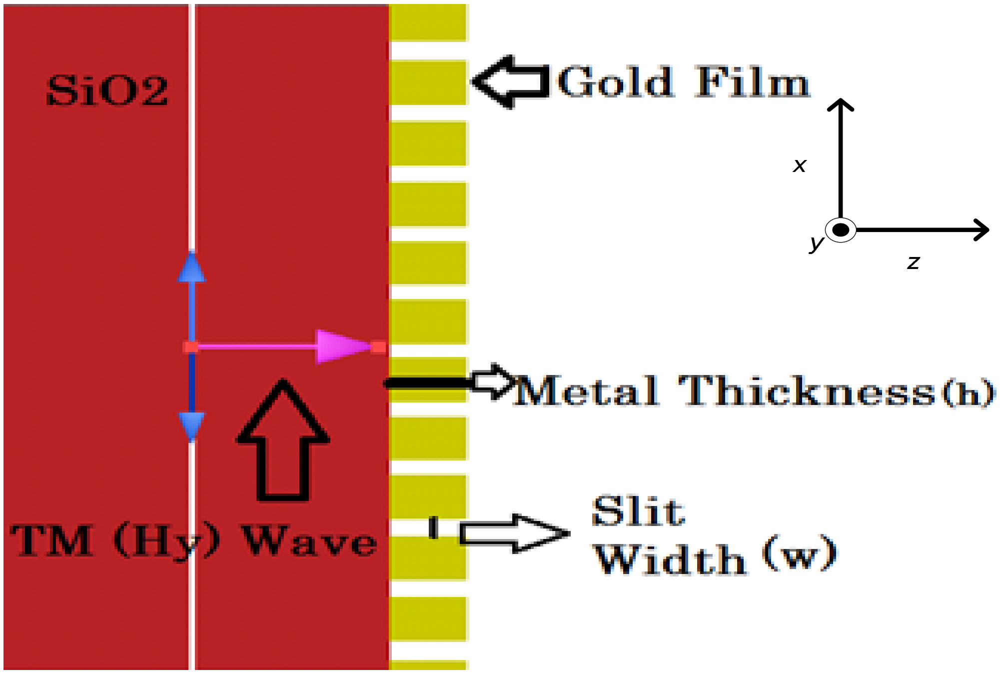

Figure 3.3 The structure of the planar slit array.

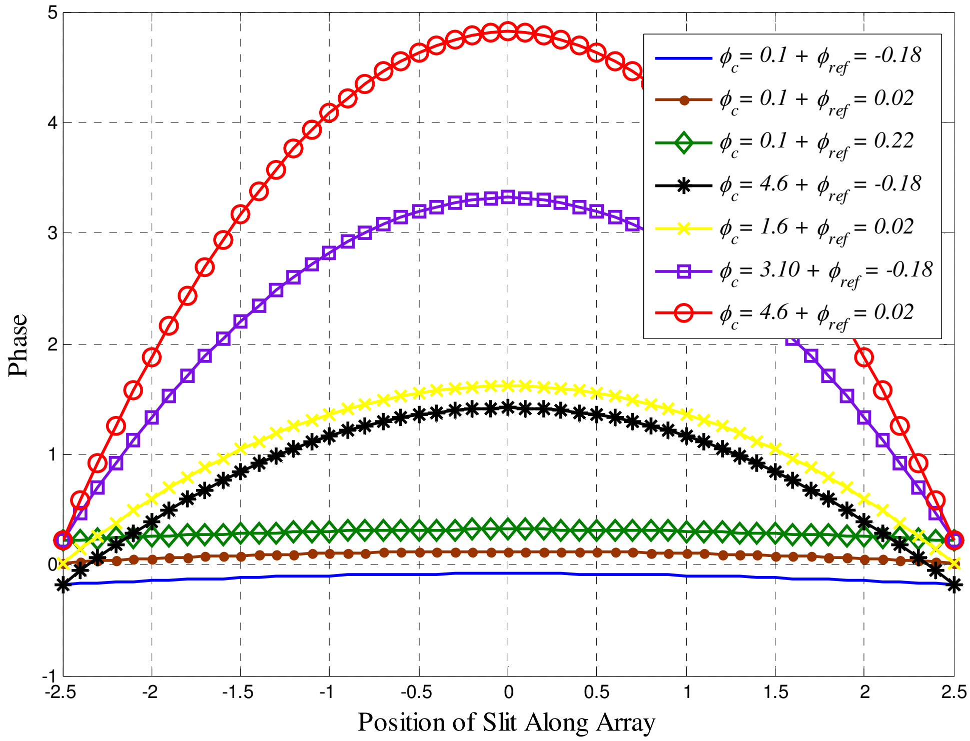

Figure 3.4 The phase profile for different values of the phase parameters ϕ_c and ϕ_{ref} .

Our target is to determine the optimal slit widths $\boldsymbol{w} = [w_1\ w_2\ \ldots\ w_N]^T$ that produces the furthest focal length (FL) and minimum beam width (BW). Taking advantage of symmetry, the number of optimization variables N is reduced. For example, in an array of 13 slits, there are only 7 optimization variables. Our target is to maximize the focal length while maintaining a reasonable beam width of BW < 1.1 μm. Our design problem is thus cast as:

$$\begin{aligned}\min_{\boldsymbol{w}} \ & -\alpha FL - \log\left(1-\frac{BW}{1.1}\right) \\ & w_i > \delta, \quad i=1, 2, ..., (N+1)/2 \, . \end{aligned} \tag{3.2}$$

Where α is a positive scaling factor. Notice that maximizing a number is equivalent to minimizing its negative. The parameter δ is the minimum slit width that is achieved by existing fabrication technology.

Equation (3.2) attempts to solve directly for the unknown slit widths. The constraint on the beam width is included within the objective function. A logarithmic barrier function [62] is used to ensure that the constraint on the beam width is satisfied. When the beam width is greater than 1.1 μm, the objective would return an exponentially increasing value to avoid the solver from stopping at a complex value. The number of optimizable parameters in (3.2) is large depending on the number of slits. Due to the curse of dimensionality, (3.2) may also be trapped into a local minimum that does not meet the design constraints. The number of required time-intensive simulations also increases by increasing the number of optimizable parameters.

In our approach, we aim at directly designing the phase profile of the structure. This drastically reduces the number of optimization parameters to the coefficients of a simple profile equation. This profile should be parabolic to achieve the focusing effect [53]. The phase constant ϕ_c represents the light phase at the center of the slit array. It controls the minimum slit width. The offset reference ϕ_{ref} alters the phase at the edges of the array to control the maximum slit width. The required phase of each slit is found from the parabolic profile. Fig. 3.4 shows the phase profile for different values of the parameters ϕ_c and ϕ_{ref} .

An alternative formulation of the optimization problem is thus proposed as:

$$\begin{aligned} &\min_{\phi_c,\phi_{ref}} \quad -\alpha FL - \log(1-\frac{BW}{1.1}) \\ &s.t. \qquad 0.1 \le \phi_c \le 3 \\ &\qquad -0.18 \le \phi_{ref} \le 0.36 \end{aligned} \quad . \tag{3.3}$$

The constraints on ϕ_c and ϕ_{ref} are employed to have a maximum and minimum slit widths of 210.0 nm and 30.0 nm, respectively. For every value of the phase offset ϕ_{ref} added to the phase constant ϕ_c, the phase of the *i*th slit (P_i) is found using the parabolic phase curves (See Fig. 3.4). The width of the *i*th slit (w_i) is then found using the formula [53]:

$$\begin{aligned} &\beta_i = \frac{P_i}{h} \\ &tanh(\frac{w_i\sqrt{\beta_i^2 - k_0^2}}{2}) = -\frac{\sqrt{\beta_i^2 - k_0^2\varepsilon_m}}{\varepsilon_m\sqrt{\beta_i^2 - k_0^2}} \end{aligned} \quad . \tag{3.4}$$

Where h is the metal thickness, which is assumed to be the same for all slits. β_i is the propagation constant of the ith slit. k_0 is the free space propagation constant, ε_m is the permittivity of the metal, and ε_d is assumed to be one for the dielectric material being air. The phase of the light transmitted through the film is given by [53]:

$$P_i = P_0 + \Delta P_1 + \Delta P_2 + \beta_i h - \theta \quad . \tag{3.5}$$

P_0 is the initial phase at the entrance; ΔP_1 and ΔP_2 are the accompanied phase changes at the entrance and exit interfaces, respectively. $\beta_i h$ is the phase retardation of the SPP waves in the slit, and θ is the term from the multiple reflections occurring in the slit. The term $\beta_i h$ is the most dominant term in calculating the phase P_i from (3.5), and thus its use in (3.4). In the TLM simulation, we use a mesh cell of $\Delta x = \Delta z = 20.0$ nm. The simulation time of this structure is 45 minutes on a 2.26 GHz PC with Intel Core i5-430M processor.

3.3.2 Results

Our TLM-based in-house simulator is implemented in Matlab [63]. We carry out a number of experiments for 13, 15, 17, and 19 slit arrays. The Matlab function *pattern-search* is used to solve the optimization problem (3.3). The *pattern-search* algorithm does not require any sensitivity information (derivatives). Our approach produces slit widths in tens of nanometers to avoid small slit changes. We simulated the array, consisting of 13 slits, for a various number of the parameters ϕ_c and ϕ_{ref} to identify the region that produces the optimal point. From this region we find the efficiency of our approach. Figure 3.5 shows that the optimal point for a beam width below 1.1 μm is produced when ϕ_c and ϕ_{ref} is 0.5 and -0.18 respectively. Thus it is expected that our approach is to produce optimal values around this region.

For all the slit arrays, the initial values for the parameter ϕ_c and ϕ_{ref} are 0.1 and 0.1, respectively. These starting parameters are chosen to produce an unfocused beam to test the efficiency of this approach. Table 1 displays the initial beam width, number of iterations, function evaluations, optimal beam width, and the optimal focal length at a beam width under 1.1 μm. As expected, our approach produces an optimal point with ϕ_c and ϕ_{ref} being 0.475 and -0.119 respectively. Figure 3.6 illustrates the achieved increase in focal length when increasing the number of slits, while keeping the beam width below 1.1 μm.

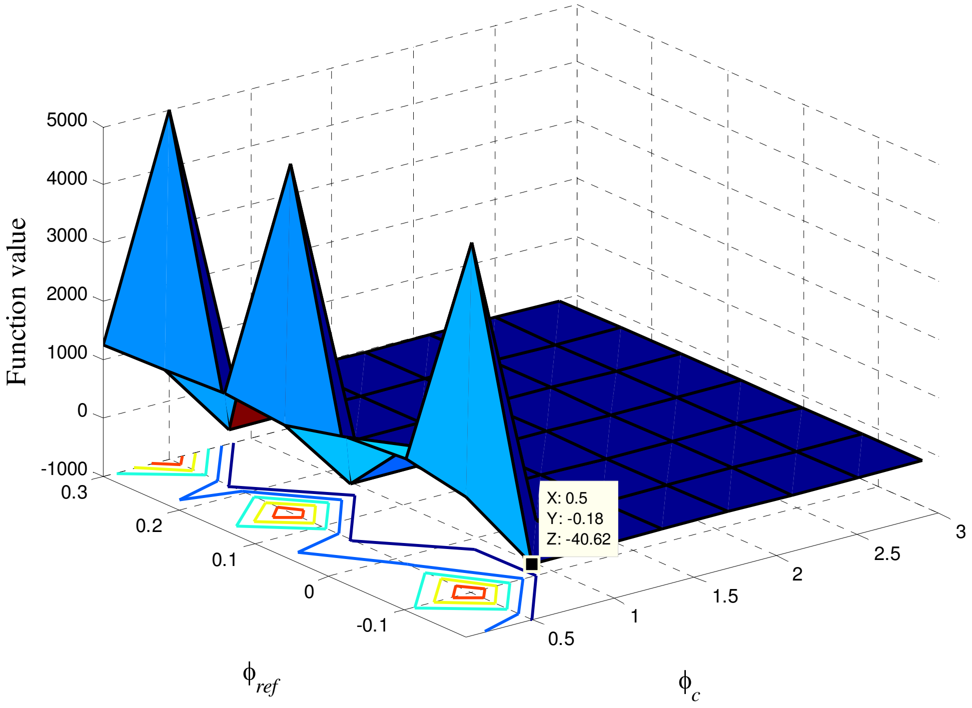

Figure 3.5 The function value plot of a 13 slit array, for different phase parameters.

Table 3.1 The starting parameters and the optimal results for different number of slits in the slit array

# of slits	Initial beam width	# of iterations	# of function evaluations	Optimal Beam width	Optimal Focal length	ϕ_c Optimal	ϕ_{ref} Optimal
13	1.32 µm	27	90	1.08 µm	7.80 µm	0.475	-0.119
15	1.52 µm	27	93	1.04 µm	8.48 µm	0.725	-0.134
17	1.66 µm	36	102	1.06 µm	9.32 µm	1.011	-0.122
19	3.74 µm	33	103	1.08 µm	10.14 µm	1.582	0.139

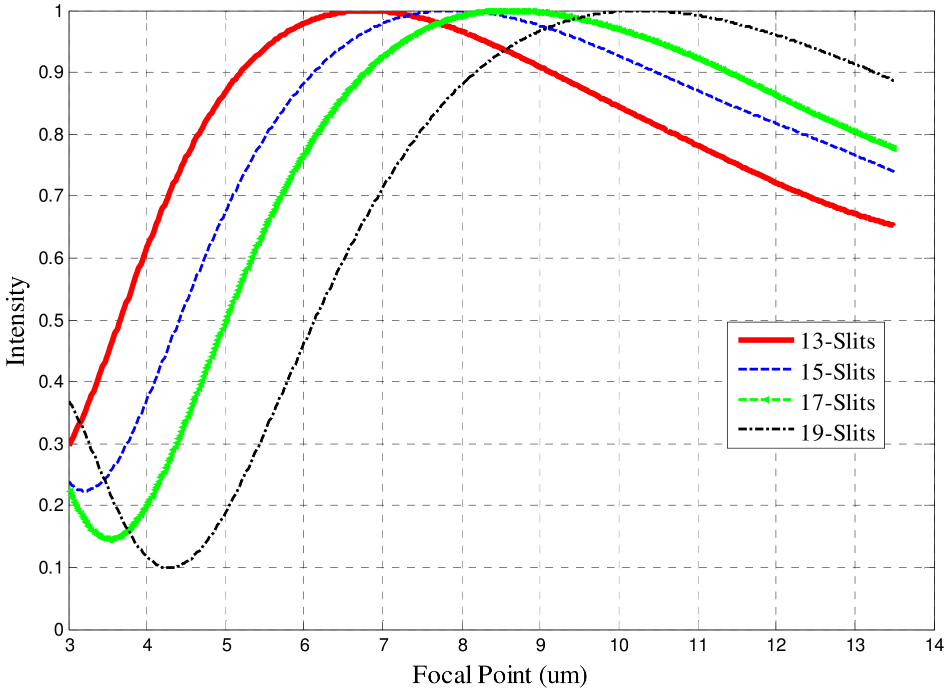

Figure 3.6 The achieved Focal length for different slit widths. (Red) the plot for 13 slits, (Blue) plot for 15 slits, (Green) plot for 17 slits, and (Black) plot for 19 slits

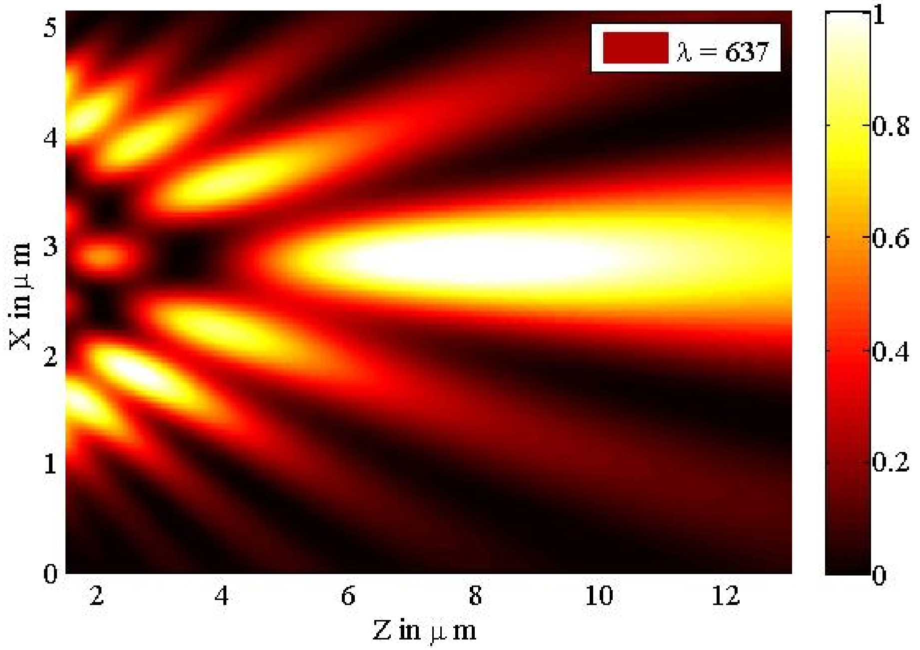

Figure 3.7 The intensity plot for the 19-slit case having a focal point at 7.68 μm with a beam width of 0.78 μm.

We also applied our approach to achieve the furthest focal length with a beam width below 0.8 μm for the 19 slit array case. We performed the same procedure and chose the initial values for the parameter ϕ_c and ϕ_{ref} to be 0.1 and 0.1, respectively. These initial values give a focal length of 13.6 μm and a beam width of 3.74 μm, which is an unfocused beam. After 33 iterations we reached an optimal design of ϕ_c = 2.94 and ϕ_{ref} = -0.116. The widths at this optimal design are given by $\boldsymbol{w}$ = [0.1900, 0.0800, 0.0600, 0.0500, 0.0400, 0.0400, 0.0300, 0.0300, 0.0300, 0.0300, 0.0300, 0.0300, 0.0300, 0.0400, 0.0400, 0.0500, 0.0600, 0.0800, 0.1900]^T μm. The focal length and beam width at this design are 7.68 µm and 0.78 µm, respectively, as seen in Fig. 3.7. Our optimal design is better than the one conveyed in [54] where a focal length of 5.3 µm and a beam width of 0.88 µm are obtained. The beam width obtained in our design is compared to that in [54] and the results are shown in Fig. 3.8.

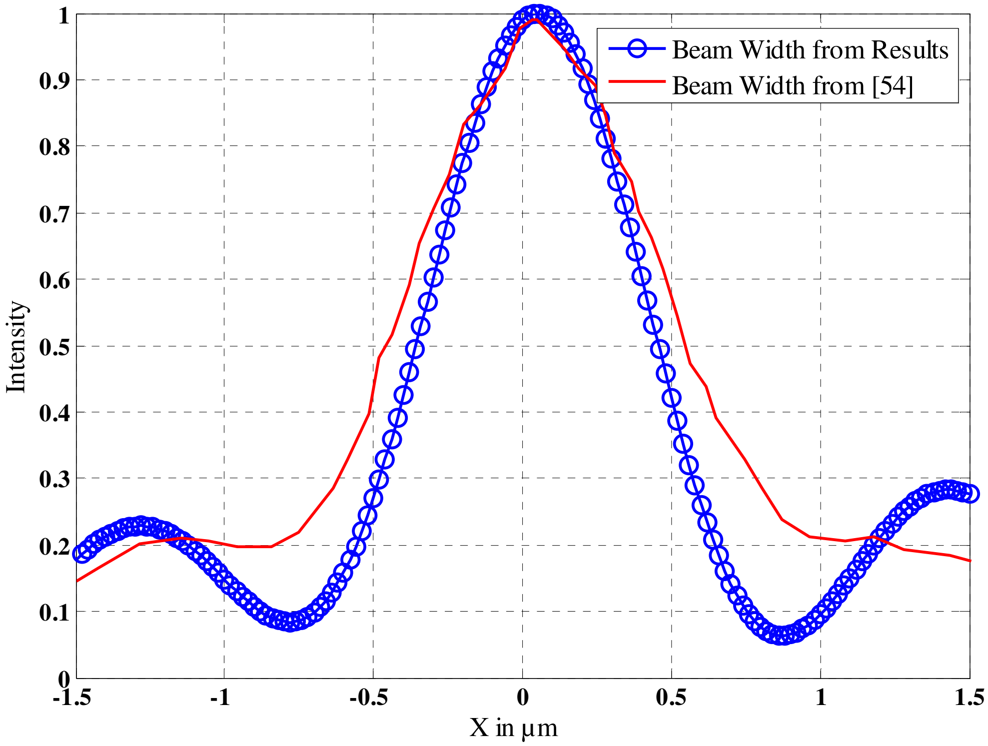

Figure 3.8 Beam width comparison between the proposed design and the design obtained in [54]. (Red-line) is the beam width obtained in [54]. (Circle-blue) beam width from our design.

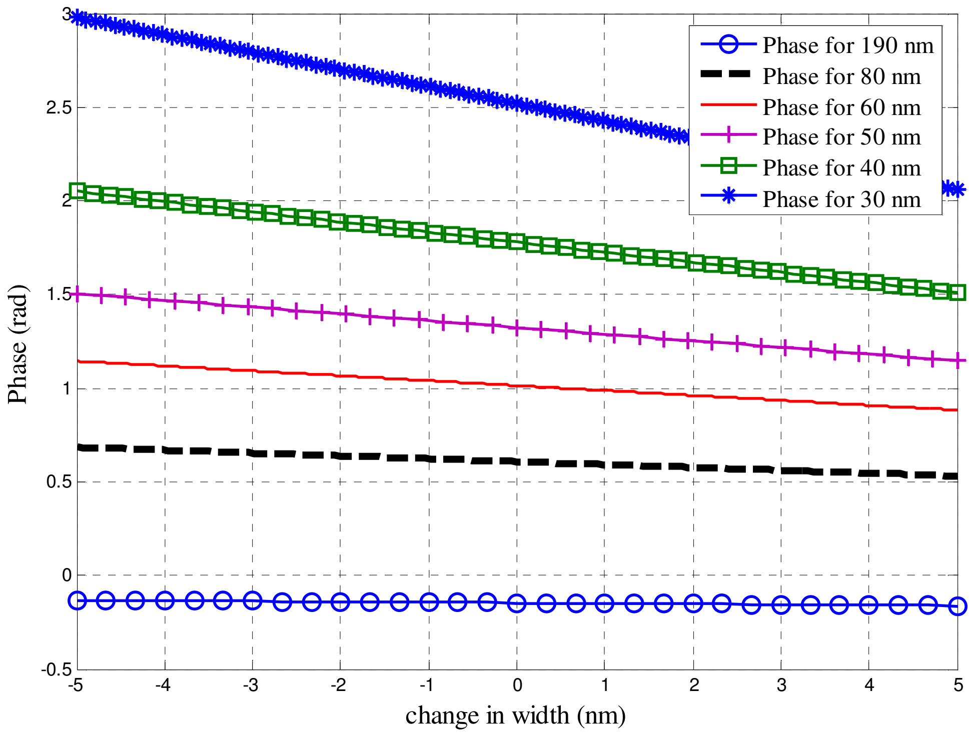

Figure 3.9 The change in phase for ±5 nm change in the optimal slit widths.

We carry out a tolerance study on the achieved design to check the robustness of the design against variations in the slit widths. We calculated the phase of the slits for a change of ± 5 nm in the slit width. Figure 3.9 shows that for large slit widths the phase does not have large variations. As the slit widths get smaller, the phase variations start to increase. Thus, much care should be given to the smaller slits when fabricating such structures.

To verify our results, the optimal 19-slit structure is modeled using Lumerical's FDTD Solutions [61]. We used the same meshing used in the

TLM simulation. The results obtained, shown in Fig. 3.10, show that the focal length is 7.63 μm and the beam width is 0.776 μm. The results have a reasonable agreement with our TLM-based results. The minor difference may be attributed to the difference between the two numerical approaches and the accuracy of each technique.

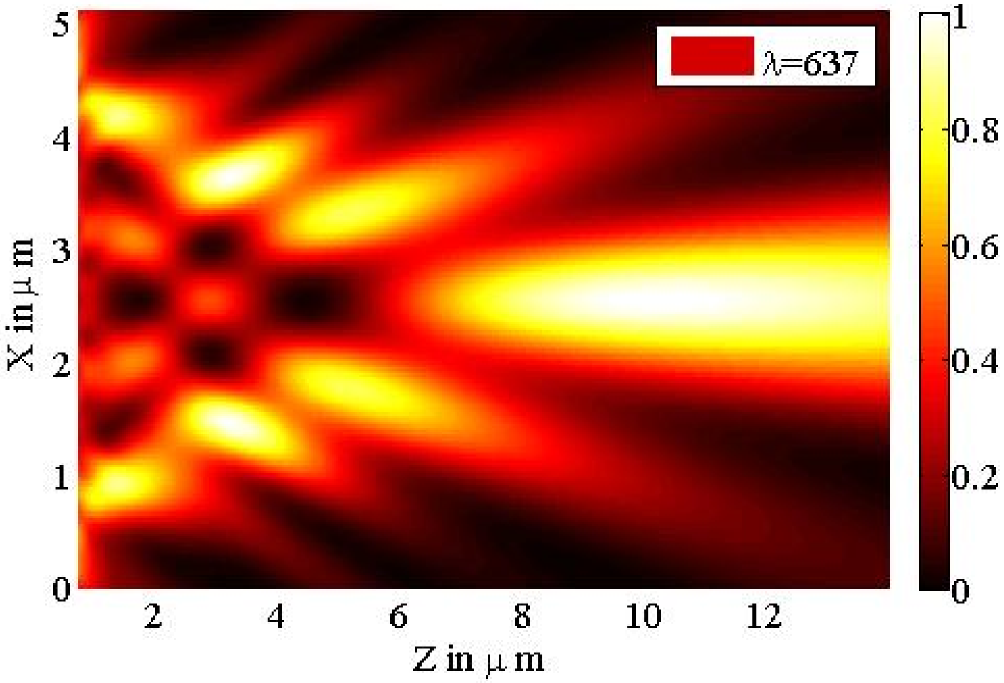

Figure 3.10 The intensity plot for 19 slit case obtained using Lumerical's FDTD Solutions (Matlab plot).

3.4 Conclusion

In conclusion, we gave an introduction to plasmonic lenses and nano-focusing. The beam focusing effect is illustrated, and the various methods for achieving lens effect are demonstrated. Moreover, various applications for the use of plasmonic slit arrays, grooves, and holes are demonstrated. Finally, a novel technique for the optimization of plasmonic slit arrays using a simple parabolic phase profile was exemplified. This technique produced slit widths by obtaining the optimal phase profile that produced the targeted criteria.

Chapter 4

Excitation of Multilevel Plasmonic Nano-Circuits Using Single Silicon Nano-wire

4.1 Introduction

In this chapter, an overview on 3-D chips and polarization splitters is demonstrated. The need to realize 3-D chips and its importance to the enhancement of performance and efficiency is highlighted. Moreover, a novel multilevel coupling technique is proposed to aid in the realization of 3-D plasmonic chips.

We start by giving an introduction to 3-D chips and polarization splitters in Section 4.2. Then a review of the background for the proposed devices is given in Section 4.3. The proposed structures are presented in Section 4.4. The results obtained using the FDTD method are shown in Section 4.5. Finally, the conclusions are discussed in Section 4.6.

4.2 3-D Chips and Polarization Splitters

In nano-scale, electronic interconnects which provide connectivity to and from fast transistors, suffers from increased delays and limited scalability. The overall speed of the system is thus limited [1], [64] due to radiation from the wires, cross-talk between the wires, and increase in effective resistance [2]. To overcome these issues, scaled down optical interconnects that provide 1000 times the data rate, longer transmission distances for data, and no power consumption per bit have been proposed [5]. However, their scalability is limited by the diffraction limit, and the large mode mismatch between optics and electronics. SPPs offer the crucial answer to these problems. SPPs enjoy the advantages of both technologies such as the scalability of electronics and the data capacity of optics, while not suffering from any of their drawbacks.

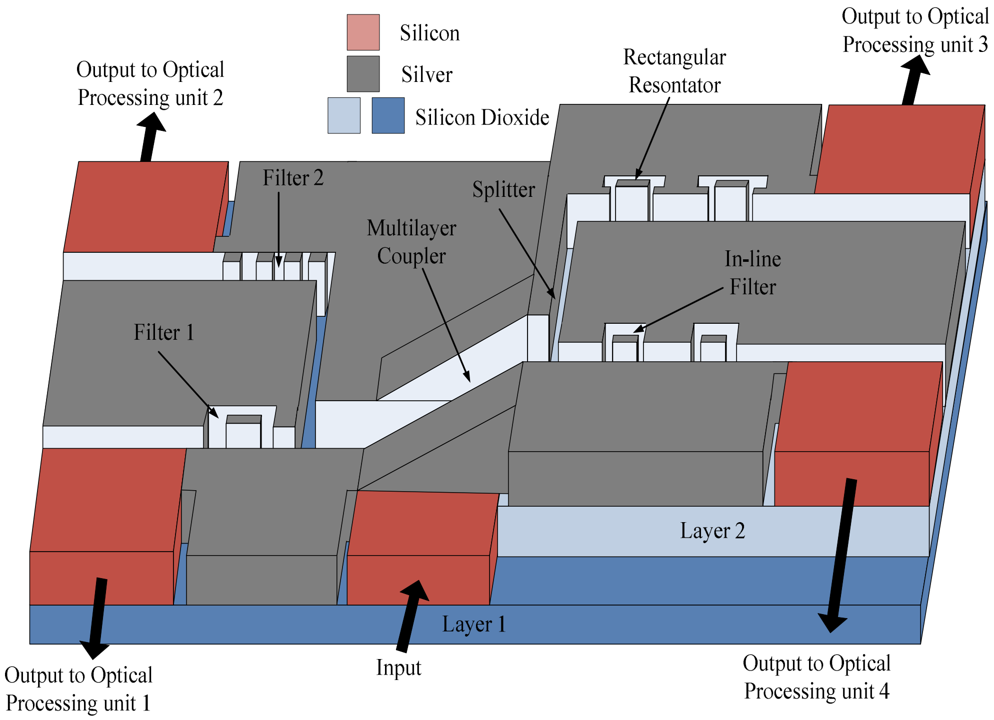

Figure 4.1 A 3-D plasmonic chip.

The interfaces between electronic and optical components are challenging for high density of integrated devices. An all optical signal processing can be exploited to realize a complete optical computation and communication system. The number of optical components placed on a chip is limited by cross talk between the closely placed components [65], [66]. In-plane chips are restricted by the size and the number of components that can be placed. Moreover, it is difficult to perform simultaneous operations on the same planar chip. An approach to solve this issue is stacking the optical chips in order to have multiple levels as shown in Fig. 4.1. By stacking multiple circuits, highly dense photonic optical circuits with faster processing and wider functionality can be realized. Different operations can be performed simultaneously without the dependence on the other levels. This is achieved if the input energy can be split between the levels. That is each layer is specialized in its own role. Moreover, this reduces the wiring distance between components, thus reducing delays [5], and increasing the overall system efficiency. Due to their compatibility with microelectronic fabrication processes, silicon photonics can help us foresee monolithic integration with the chip multiprocessor and on-chip memory in the 3-D stacks [5].

Several approaches for realizing 3-D optical chips have been proposed [65]-[68]. These devices include optical multiplexers, multimode interferometer, splitters, switches and waveguides [65]-[72]. However, the devices are designed using the conventional silicon on insulator (SOI) waveguides. This makes them limited in both band and size and subject to cross talk. Similarly, these devices are very sensitive to wavelength alterations and fabrication [66]. A promising alternative is to exploit plasmonic circuits to provide high density integration with minimal cross talk. However, little work has been done in realizing 3-D chips using plasmonics. The device presented in [73] uses long-range surface plasmon polaritons (LRSPP). This device is long and its operation is limited by its length. In addition, so far 3-D plasmonic chips are limited to the inherent polarization dependence of the surface plasmon polariton waves. Signal manipulation utilizes only one polarization of the input field. The other polarization does not couple to the SPP structures. This is considered a serious draw back that hinders using quadrature functionalities.

Recently few on-chip plasmonic polarization splitters [74]-[77] and polarizers [78], [79] are proposed for quantum electrodynamics [80], and for logic gates [81]. This dramatically reduces the size of an optical chip. However, all of the proposed structures are in-plane, and the splitting is only done at one layer. Besides, special care is needed when designing and manufacturing these splitters due to the fine tapering and positioning. The splitting ratio is dimension-dependent which makes it very sensitive to the fabrication process.

In the following sections, we propose a novel structure for realizing multilevel plasmonic chips based on the plasmonic slot waveguide (PSW) configuration demonstrated in [24]. This structure, in addition, acts as a surface plasmon polarization beam splitter. The main functionality of this device is to allow both polarizations of the input fields to be manipulated using plasmonic structures by routing each one to a different level. A conventional silicon nano-waveguide is employed as the input waveguide. By controlling the light polarization at nano-scale, on-chip communication will be much faster. In addition, optical digital gating functionality can be developed.

Moreover, this will introduce a quadrature space that provides multifold of the current capacity. The proposed device helps in realizing 3-D plasmonic chips that are compact and with high integration and density. Two variations of the suggested structure are investigated. In the first one, the two plasmonic waveguides are orthogonal. In the second one, one of the plasmonic waveguides is rotated to allow light propagation in a parallel horizontal plane. These devices are wideband and ultra-compact with realizable dimensions. The Finite difference time domain (FDTD) technique is utilized to verify the operation of the two devices. The polarization splitting capability of these structures can be utilized in linear optics, multiplexers, logic gates [75], [76], or optical interconnect applications.

4.3 Background for Orthogonal Coupling

The proposed multilevel devices are based on orthogonal coupling between silicon waveguides and PSWs. Utilizing the polarization-dependent nature of the plasmonic slot we can separate the two different polarizations. Orthogonal orientation between the silicon and plasmonic waveguides not only allows for polarization splitting but has been proven to provide efficient coupling [24]. This allows for simultaneous efficient coupling to different layers of a 3-D plasmonic chip and polarization splitting.

For the plasmonic slot waveguide shown in Fig. 4.2, distinct modes are allowed to propagate [25]. These modes are determined through a numerical solution of reduced Maxwell's equations in the magnetic field [25]. Figure 4.3 shows the fundamental TE mode that propagates in the PSW [78]. When the slot is perpendicular to the *x*-axis (as shown in Fig. 4.3), the fundamental mode having a dominant E_x and H_y fields propagates. When the slot is perpendicular to the *y*-axis, the dominant mode has E_y and H_x components. Throughout this paper, we refer to the modes having a dominant E_x and H_y fields as *x*-polarized (quasi-TE mode), and modes having a dominant E_y and H_x as *y*-polarized (quasi-TM mode).

The PSW demonstrated here is made up of silver with a silicon dioxide substrate [82], using the model presented in Lumerical [61]. The cell size is $\Delta x = \Delta y = 2.0$ nm and $\Delta z = 5.0$ nm since the mode of interest is perpendicular to the *z*-direction. The width and height of the PSW are 340.0 μm and 400.0 μm, respectively. Figure 4.3 demonstrates the mode profile for the *x*-polarized mode, which propagates along the *z*-direction. It is obtained using Lumerical's mode solver [61]. The mode solver solution is normalized with respect to the maximum field intensity.

Several approaches for coupling energy into plasmonic waveguides have been suggested. The direct coupling is done by connecting the dielectric waveguide to the plasmonic slot waveguide. Figure 4.4 illustrates the transmission properties using direct coupling. This figure is created using the same computational information mentioned above, with a detector placed around the slot, 300.0 nm away from the interface. The excitation in the Si waveguide is done by injecting it with a Gaussian-modulated sinusoidal that spans the wavelengths 1.1 µm – 2.5 µm. In Fig. 4.4, the *x*-polarized mode, from the input silicon waveguide, is allowed to propagate in the plasmonic waveguide while the *y*-polarized mode is completely reflected. The mismatch between the silicon waveguide and the PSW reduces the coupling efficiency as evident from Fig. 4.4.

It is difficult to separate both the *x*- and *y*-polarized modes simultaneously. To separate both the polarizations, s-bends or branches [77] are required. This introduces losses and fabrication complexities. The mismatch between the silicon waveguide and the PSW reduces the coupling efficiency (see Fig. 4.4). The transmission of such a structure suffers from oscillatory responses, when coupled to and from silicon waveguides [24]. This introduces distortions and reduces the band for efficient operation.

The enhanced performance of the right angle coupling between the dielectric waveguide and the PSW was validated in [24]. This right angle coupling provides higher polarization selectivity with minimal coupling losses and enhanced bandwidth. It also provides a wideband modal matching and thus a better coupling efficiency. The modal compatibility between plasmonic and dielectric waveguides is better illustrated through the analysis of the propagation constant (*k*) [24].

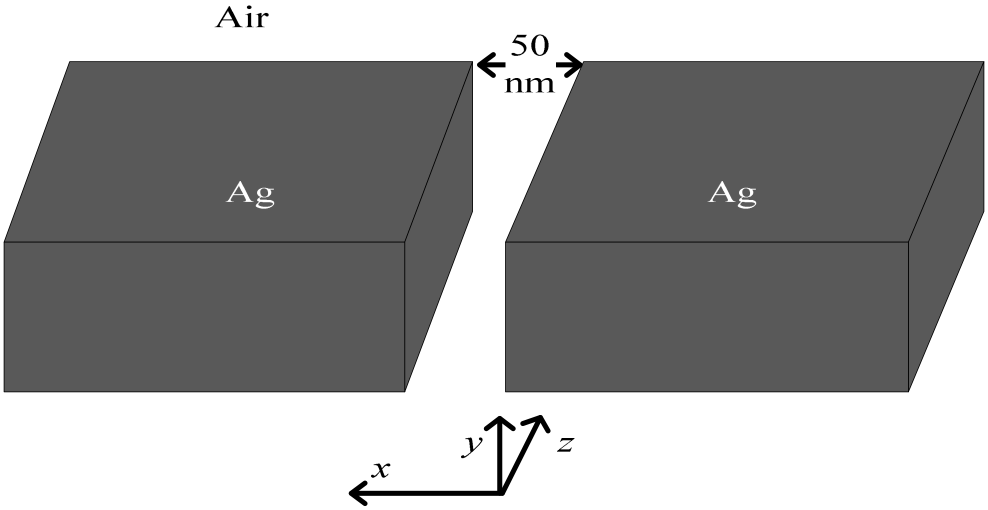

Figure 4.2 A plasmonic slot waveguide with air as the dielectric present in the slot.

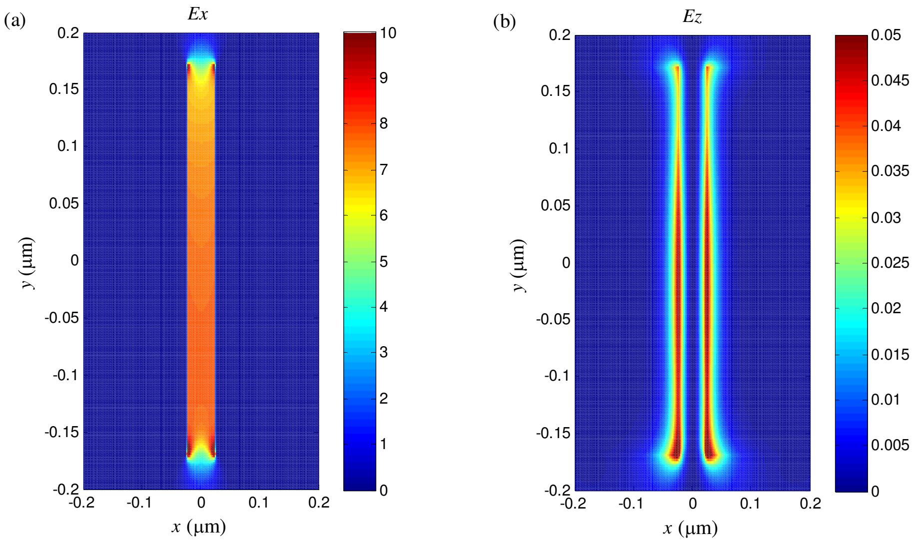

Figure 4.3 Cross sectional view of the PSW demonstrating (a) E_x present in a plasmonic slot waveguide and (b) E_z present. The slot width is 50.0 nm.

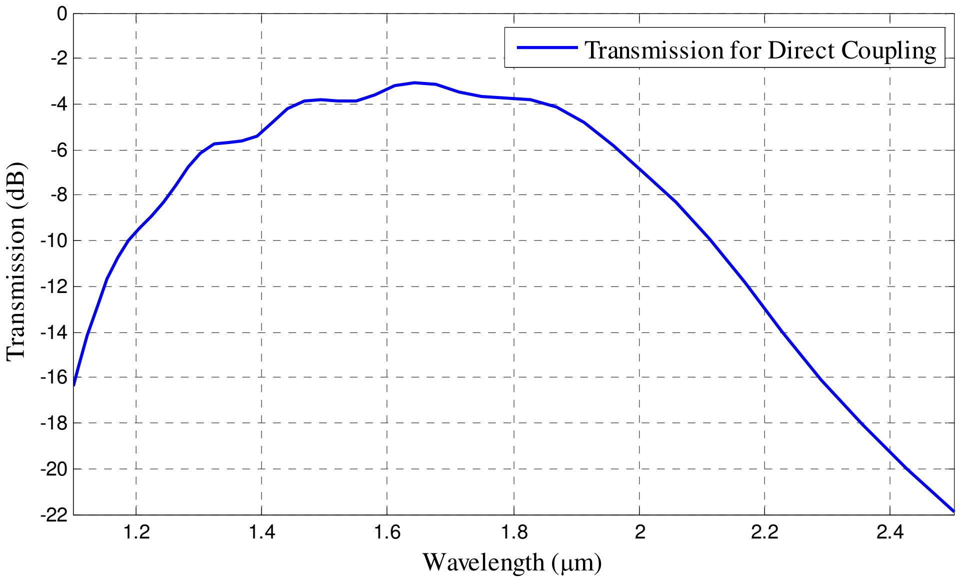

Figure 4.4 Transmission plot for the direct coupling method for a slot width = 50.0 nm.

4.4 The Proposed Structures for Polarization-Controlled Surface Multilevel Beam Splitter/coupler

Two 3-D polarization-controlled beam splitters are investigated in this work. For the first structure, the light guided by the dielectric waveguide is split using two orthogonal plasmonic slot waveguides. The second structure exploits a rotated plasmonic slot waveguide to couple the signal to a parallel horizontal plane on a different layer. In this section more details are given about the performance of the two devices.

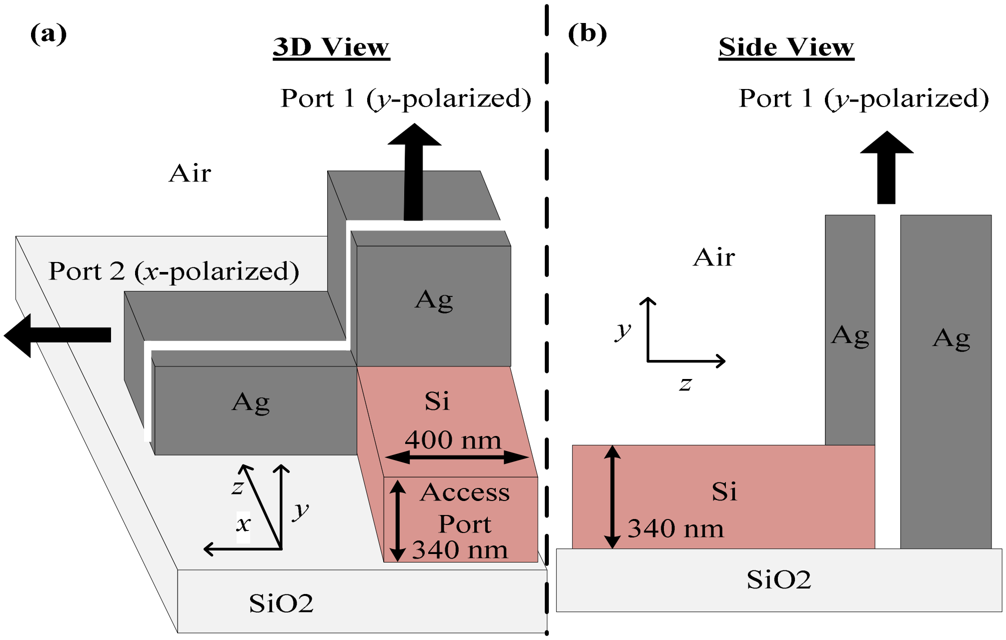

Figure 4.5 The proposed orthogonal polarization splitter configuration;(a) 3D view and (b) side view.

4.4.1 The Orthogonal Polarization Splitter

We first propose a novel multilevel polarization splitter from a silicon waveguide to PSWs. The proposed structure exploits the orthogonal coupler presented in [24]. This coupler is polarization dependent and allows one polarization only (*x*-polarized wave) to couple to the PSW. However, slight modification demonstrates that this coupler can couple both polarizations but at different planes. The proposed coupler is shown in Fig. 4.5. The input waveguide is a silicon nano-wire with dimensions of 340.0 x 400.0 nm fabricated using SOI wafer. The dimensions of the PSW with a 50.0 nm slot are one order of magnitude less than that of the dielectric waveguide. The advantage that PSWs supports only one polarization is exploited in order to setup the device. The principal of operation of this device is to split the two polarizations existing on the dielectric waveguide with each polarization coupling to only one of the two orthogonal PSW waveguides. Both polarizations can be processed at the same time. One polarization is guided horizontally while the other polarization is guided vertically. Each signal is then guided to its respective circuit using sharp bends with maximum efficiency [83]. Each polarization is processed and manipulated in its respective layer. The *x*-polarized (quasi-TE) mode is responsible for the operation of the horizontal or in-plane layer, while the *y*-polarized (quasi-TM) is responsible for exciting the stacked layers. This allows for quadrature modulation as well.

To illustrate the application of this device, we conduct a dispersion analysis on the proposed 3-D configuration using [17]. The dispersion relation is for semi-infinite structures, and this is taken care of in the simulations by terminating the structure with a perfectly matched layer (PML). The dispersion relationship is given by:

$$
\begin{aligned}
&\tanh k_1 a = -\frac{k_2 \varepsilon_1}{k_1 \varepsilon_2} \\
&k_1 = \sqrt{\beta^2 - k^2 \varepsilon_1} \\
&k_2 = \sqrt{\beta^2 - k^2 \varepsilon_2} \ .
\end{aligned}
\tag{4.1}
$$

In (4.1) $k_{1,\,2}$ are the wave-vectors in the dielectric and metal, respectively, and $\varepsilon_{1,\,2}$ are the dielectric constants of the dielectric and metal, respectively. β is the effective wave-vector and a is half of the slot size. Figure 4.6 shows that the dielectric propagation constants, k_x and k_y, have a better coordination with the PSW propagation constant, $k_{spp,}$ than with k_z. These propagation constants are obtained using the equations in chapter 2. This is in agreement with the 2-D analysis given in [24].

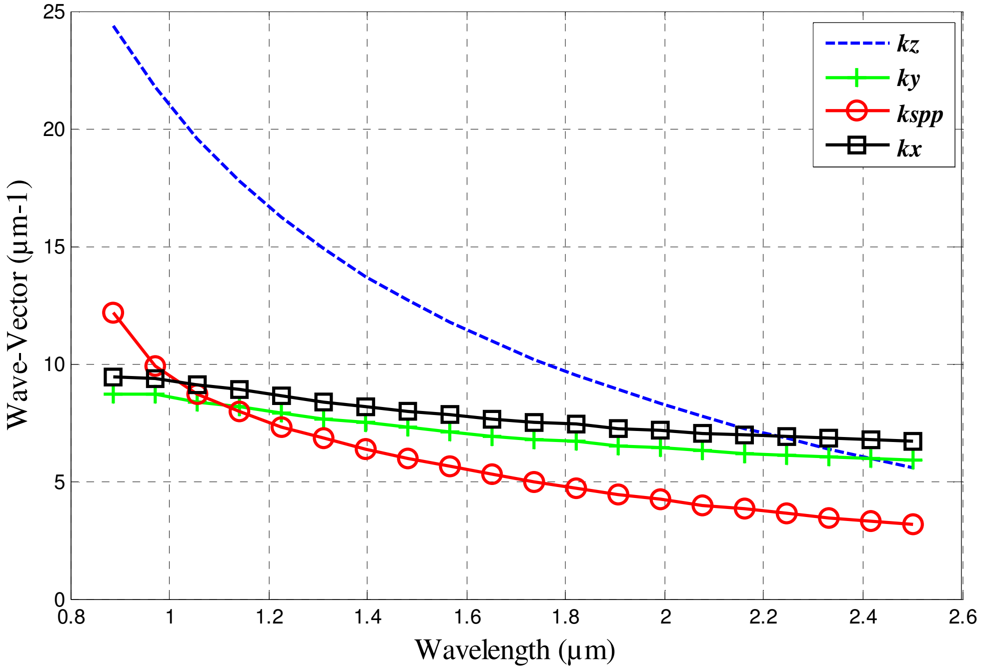

Figure 4.6 A wave-vector plot for the proposed 3D orthogonal polarization splitter. The *kx* and *ky* inside the dielectric waveguide are more closely matched to *kspp* than *kz*.

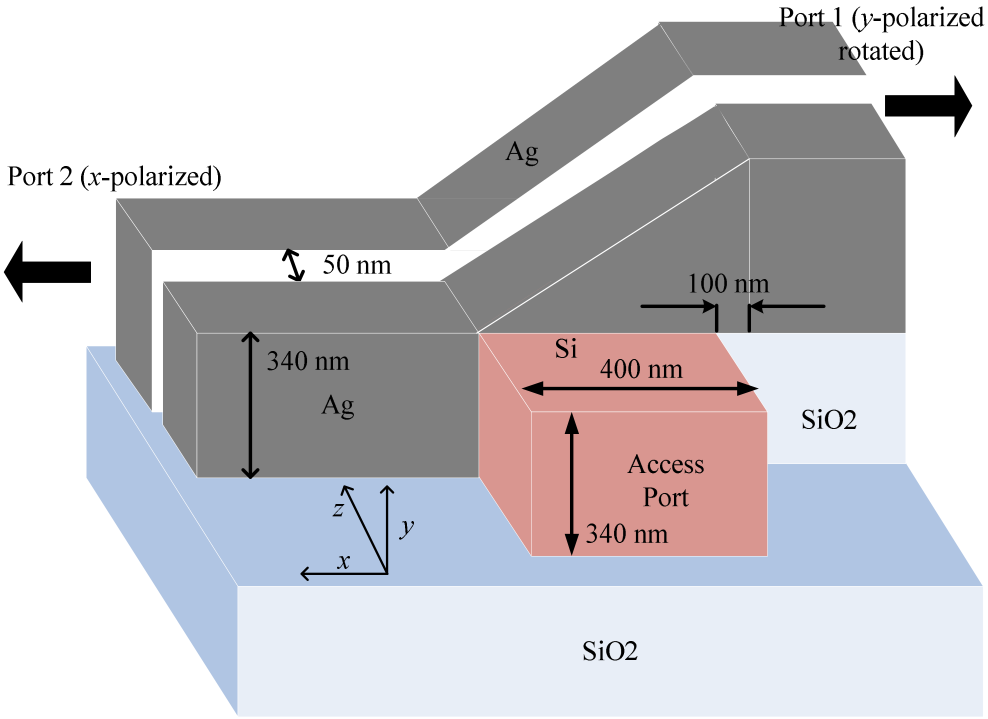

Figure 4.7 The structure of the rotated polarization splitter that couples each polarization to a different layer

4.4.2 The Rotated Splitter for Multilevel Coupling

We present a variation of the structure presented in 4.4.1 to rotate the vertically coupled beam for in-plane light processing. To achieve this goal a polarization rotator is exploited at the top of the polarization splitter. This structure uses a triangular shaped metal in the vertical direction to introduce a discontinuity to the wave. The slope of the triangle forces the wave propagating upwards to move along a path perpendicular to its original propagation. The complete structure is shown in Fig. 4.7, where the edge of the triangle is placed 100 nm to the side of the silicon waveguide. This will help in the realization of stacked layer chips. This structure acts like a *T*-junction at multiple levels and only one polarization is coupled at each of the output ports 1 and 2.

As shown in Fig. 4.7, this device works by selecting the input polarization. If the input polarization at the silicon waveguide is x-polarized, the light couples to port 2. On the other hand, if the input polarization is y-polarized, the light is coupled to port 1. Thus the light beam can be routed at different horizontal planes by choosing the corresponding polarization. This device, for the first time, allows simultaneous manipulation of the two polarizations using PSWs. The main applications of this device include quadrature modulation where each polarization is modulated at a different level. The final beam is combined again using the same device. This device demonstrates more compact and efficient use of the PSW-based applications. It can, similarly, be exploited as a selective router that controls the signal route at different layers as shown in Fig. 4.1.

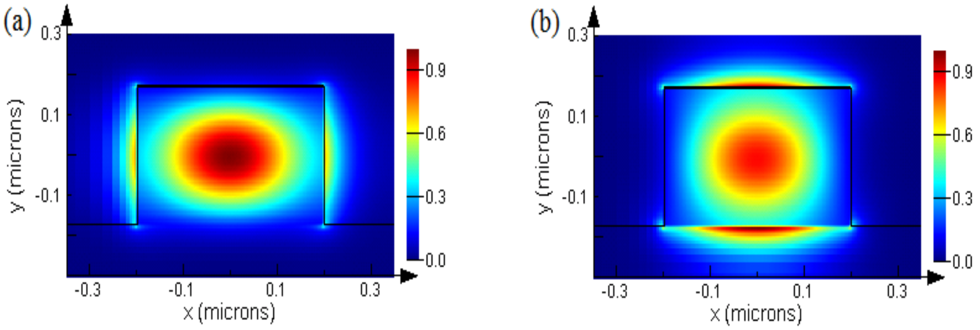

Figure 4.8 The two excitation source modes. *x*-polarization (a) and *y*-polarization (b).

4.5 Modeling and Simulation Results

The FDTD technique is used to simulate the coupling from the Si waveguide to the two orthogonal PSWs. The commercial software, Lumerical FDTD solutions [61], is utilized to simulate and analyze the two suggested structures. The metals used for the PSW are silver and aluminum [82]. The dielectric materials used for the dielectric input waveguide and substrate are silicon and silicon dioxide, respectively [82]. A high order polynomial fitting of measured data is used in dispersive FDTD [61]. The losses in all materials are given by the model used in [61]. The dielectric slot and surrounding medium used are air. For meshing the plasmonic section of the structure, a square cell of $\Delta x = \Delta y = \Delta z = 2.5$ nm is used. A perfectly matched layer (PML) is utilized to terminate the computational domain. Detectors are placed at the cross section of each PSW at a distance of 200.0 nm away from the splitting junction. These detectors probe the electric fields, magnetic fields, and transmission efficiencies in each arm. The normalized transmission is calculated by determining the power flux through the detector plane, integrating it over the cross section, and normalizing it with respect to the source power. The answer is then converted into dB using (4.2). The absorption in the metal, which is given in (4.3), is measured as well:

$$\text{Transmission(dB)} = 10\log(T)\,. \tag{4.2}$$

$$\text{Absorption(dB)} = 10\log(1 - T_1 - T_2 - R)\,. \tag{4.3}$$

Where T is the normalized transmission obtained. T_1, T_2 and R are the normalized transmissions in ports 1, 2, and the reflection, respectively. The reflection from the junction is calculated in the same way. The excitation in the Si waveguide is done by injecting it with a Gaussian-modulated sinusoidal that spans the wavelengths 1.0 µm – 2.5 µm. Each of the two dominant modes (*x*-polarized and *y*-polarized) is excited separately using the mode solver in [61]. The sources are excited at a distance of 1.5 µm from the splitting junction. The excited *x*-polarization and *y*-polarization modes in the dielectric waveguide are shown in Fig. 4.8.

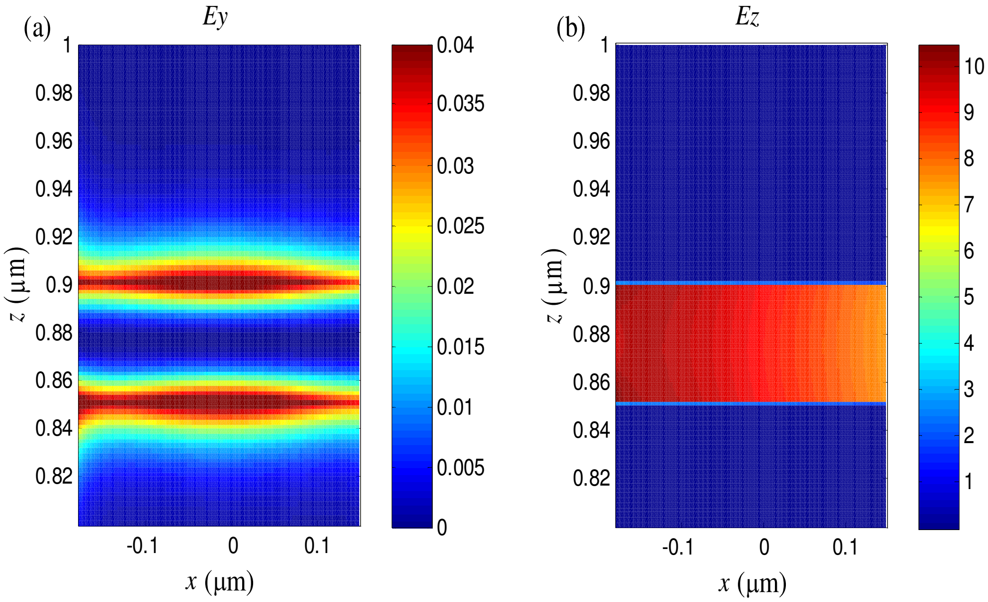

Figure 4.9 Electric fields intensity plots in port 1 when excited with a y-polarized wave at 1.55 µm.

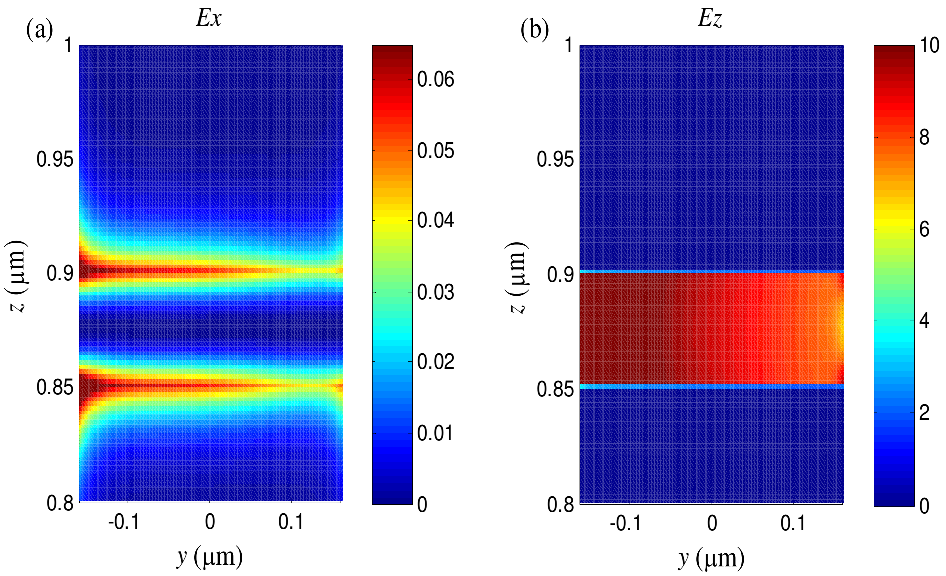

Figure 4.10 Electric fields intensity plots in port 2 when excited with an x-polarized wave at 1.55 µm.

In this section, we discuss the results obtained for both the orthogonal polarization splitter (Fig. 4.5), and the rotated polarization splitter (Fig. 4.7). For the PSW oriented in the *y*-direction (Fig. 4.5), the dominant fields are E_y and E_z. The mode profiles in this case are shown in Fig. 4.9. While for the PSW oriented in the *x*-direction, E_x and E_z are the dominant fields, with a modal profile rotated to be in the *x*–direction as shown in Fig. 4.10. For the *y*-polarized wave, the resulting fields propagate in port 1 with very little transmission to port 2. Figure 4.9 shows the most dominant field in port 1 to be the E_z field. However, it can be seen that the E_y field intensity has moderate power while propagating along the metal surface. The remaining fields present are very small compared to the dominant ones. Figure 4.10 shows that the reverse of the *y*-polarization case occurs at port 2 when the structure is excited using an *x*-polarized wave at 1.55 µm. the slight differences in the field plots is due to the uneven dimensions of the PSWs

The *y*- and *x*-polarized waves are received at port 1 and port 2, respectively. As expected, when the Si waveguide is excited with a *y*-polarized mode (discontinuity along *y*-axis), the wave propagates along the PSW oriented in the *y*-direction (port 1). The transmission is calculated at 1.55 µm in both PSWs. It is found that the *y*-oriented waveguide has -3.7 dB power transmission, while the PSW oriented in the *x*-direction has approximately -17.2 dB. This is illustrated in Fig. 4.11. The same procedure is carried out while exciting the Si waveguide with an *x*-polarized mode (discontinuity along *x*-axis). A power transmission of -3.87 dB in the *x*-oriented PSW (port 2) is achieved. A transmission of approximately -15.5 dB is obtained in the *y*-oriented PSW. The slight difference in the transmission efficiency is attributed to the non-equal dimensions of the Si waveguide. The results are demonstrated in Fig. 4.12. The extinction ratios for both ports are shown in Fig. 4.13. The extinction ratio is the power in one port compared to the other port for the two different polarizations and is given by:

$$\text{Extinction Ratio(dB)} = 10\log(\frac{T_{int}}{T_{sub}}) \quad . \tag{4.4}$$

T_{int} is the transmission in the port of interest, while T_{sub} is the transmission in the subsidiary port. Figs. 4.11 and 4.12 reveal that the absorption increases beyond a wavelength of 1.6 µm. The best band for operating this structure is between 1.4 µm and 1.6 µm. In this band the device enjoys maximum transmission as well as lower reflection and absorption as compared to other frequencies. This demonstrates the broadband feature of this structure.

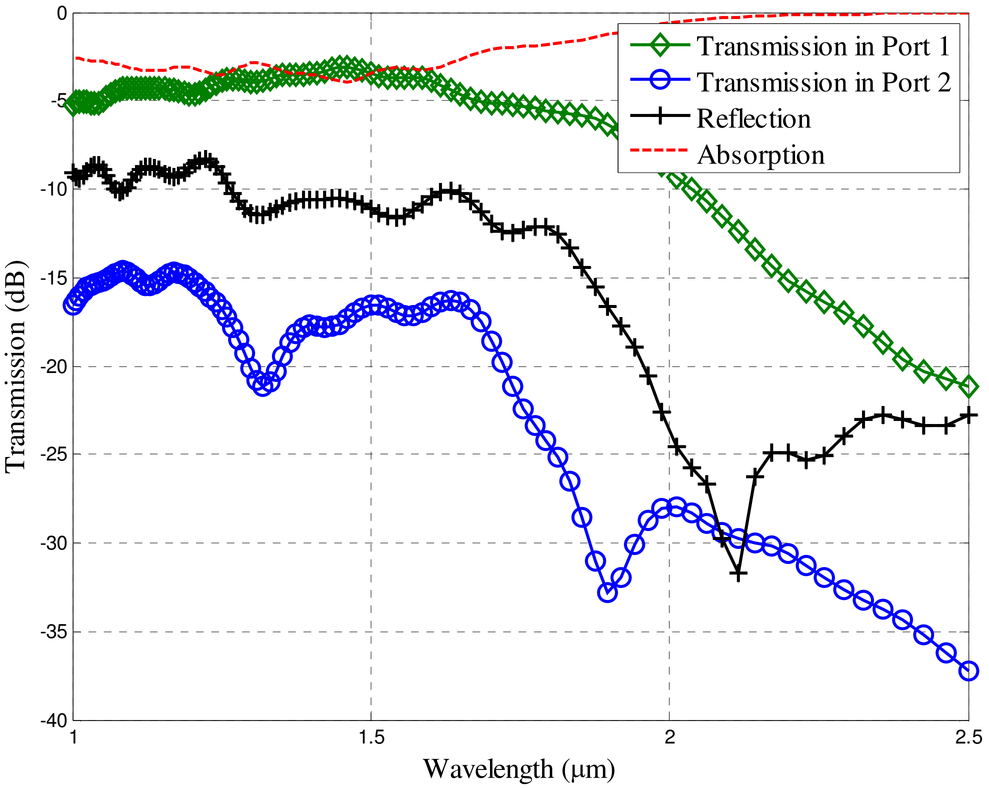

Figure 4.11 The transmission efficiency for the orthogonal polarization splitter when excited with a y-polarized mode; (Diamond-Green) is the transmission along port 1, (Circle-Blue) is the transmission efficiency along port 2, (Dotted-Red) is the absorption in the metal, and (Cross-Black) is the reflection from the junction.

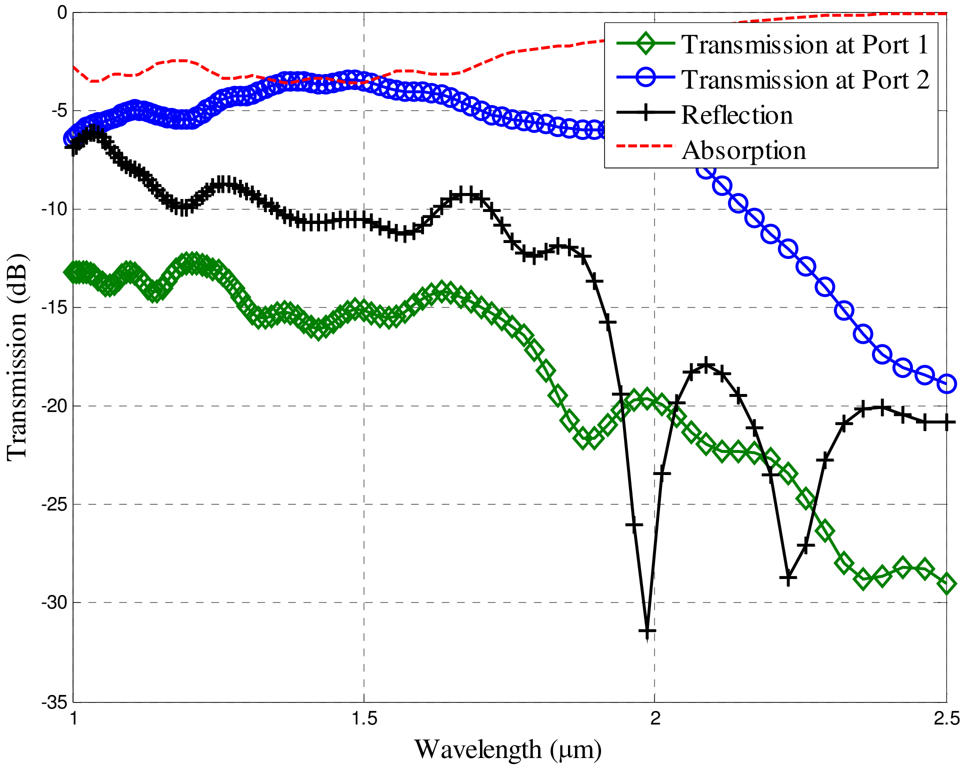

Figure 4.12 The transmission efficiency for the orthogonal polarization splitter when excited with an x-polarized mode; (Diamond-Green) is the transmission along port 1, (Circle-Blue) is the transmission efficiency along port 2, (Dotted-Red) is the absorption in the metal, and (Cross-Black) is the reflection from the junction.

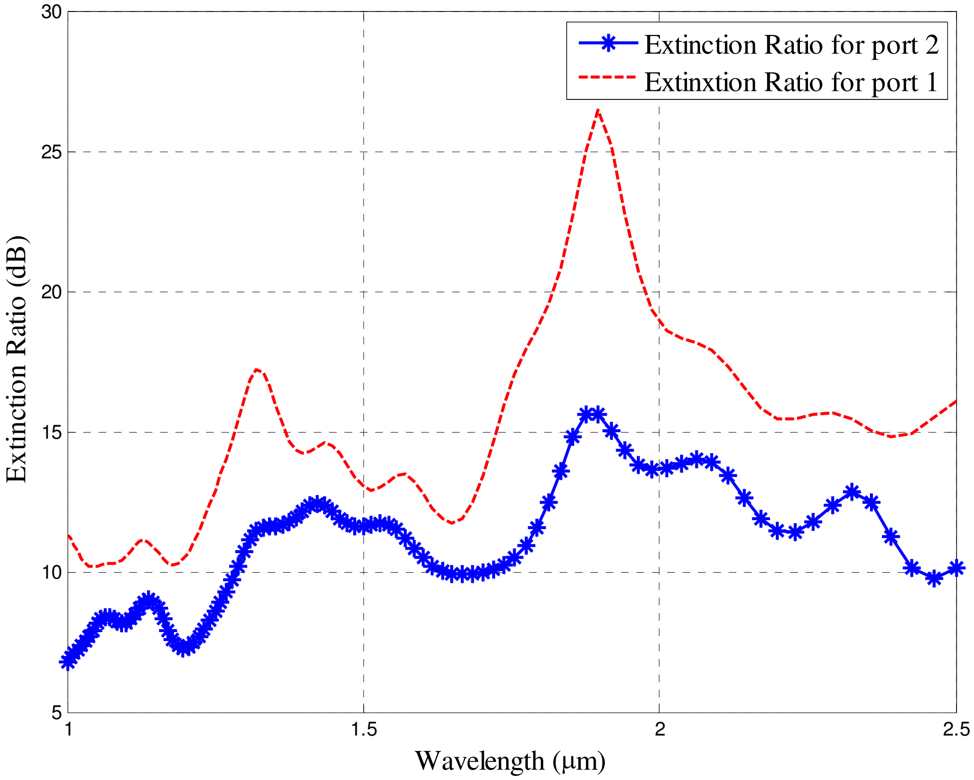

Figure 4.13 The extinction ratio for the orthogonal polarization splitter calculated for port 1 (Dotted-Red) and for port 2 (Star-Blue).

We repeat the same analysis for the rotated polarization splitter shown in Fig. 4.7. Figure 4.14 shows the transmission when the dielectric waveguide is excited with a *y*-polarized mode. Here, the transmission in port 1 is -4.7 dB, while that in port 2 is -21.1 dB. This shows that around 75.46% of the wave propagating in the vertical PSW (port 1 in Fig. 4.5) can be channeled horizontally to port 1 (Fig 4.7). Figure 4.15 shows a transmission of -4.3 dB to port 2 and -21.7 dB to port 1 when the structure is excited with an *x*-polarized wave. This shows the excellent splitting and polarization rotation functionality of the device. The extinction ratios for both ports are displayed in Fig. 4.16. The functionality of the device, when using aluminum [82] instead of silver, is also presented. The results for the *y*-polarized excitation, *x*-polarized excitation, and extinction ratio when using aluminum are displayed in Figs. 4.14-4.16 respectively. The figures show that the transmission power using aluminum is around 1 dB less than its counterpart. Furthermore, the extinction ratio for each port using aluminum is closely related to that of the silver. This demonstrates that the structure is more compatible with traditional CMOS technology based on using silicon and aluminum.

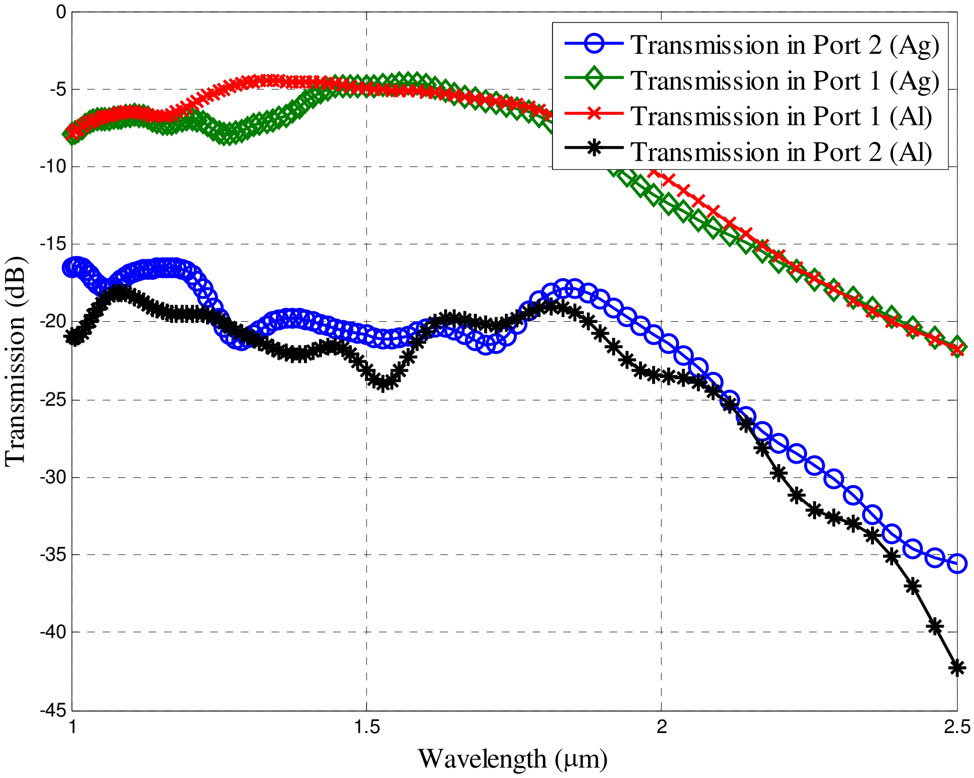

Figure 4.14 The transmission efficiency for the rotated polarization splitter when excited with a y-polarized mode; (Diamond-Green) is the transmission along port 1 for silver, (Circle-Blue) is the transmission efficiency along Port 2 for silver, (X-Red) is the transmission efficiency along Port 2 for silver, (X-Red) is the transmission along port 1 for aluminum, and (Star-Black) is the transmission along port 2 for aluminum.

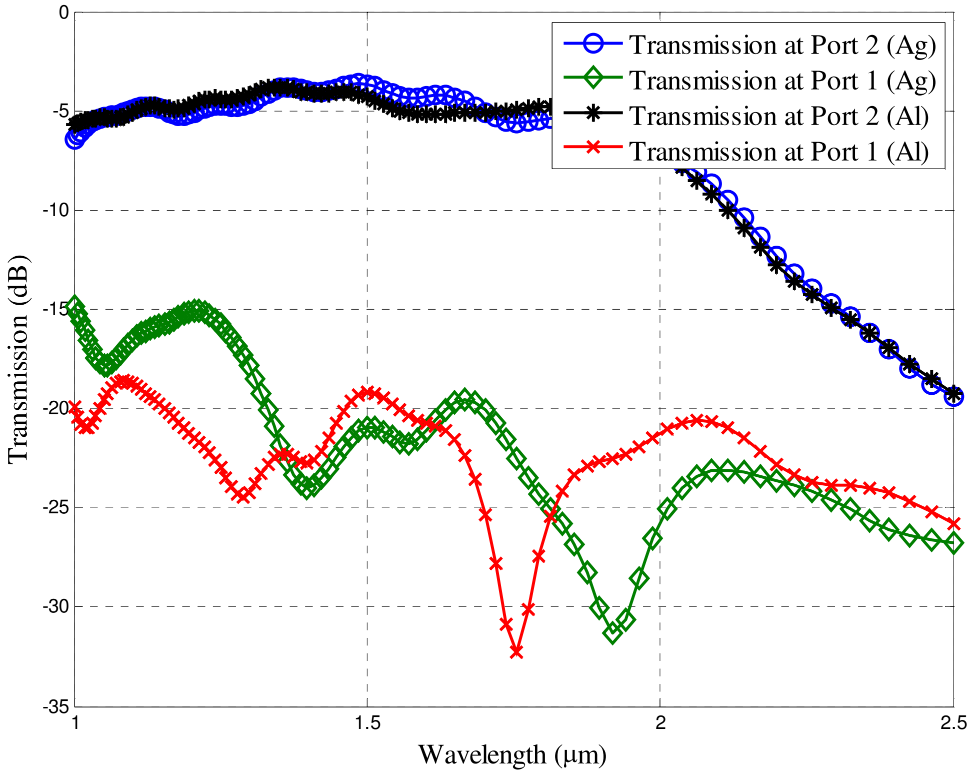

Figure 4.15 The transmission efficiency for the rotated polarization splitter when excited with a x-polarized mode; (Diamond-Green) is the transmission along port 1for silver, (Circle-Blue) is the transmission efficiency along port 2 for silver, (X-Red) is the transmission along port 1 for aluminum, and (Star-Black) is the transmission along port 2 for aluminum.

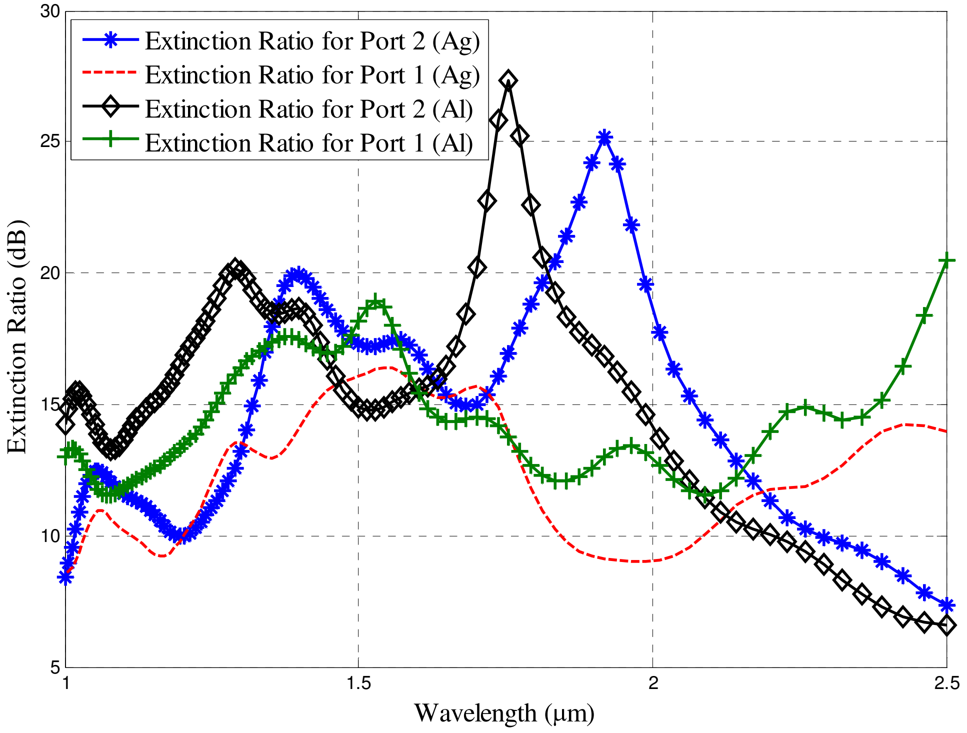

Figure 4.16 The extinction ratio for the rotated polarization splitter calculated for port 1 (dotted-red) and for port 2 (Star-blue) using silver material. (Cross-Green) and (Diamond-Black) are the extinction ratios for ports 1 and 2, respectively, estimated using *aluminum.*

4.6 Conclusion

We presented two novel SPP polarization splitters utilizing the orthogonal junction coupling technique. The first structure exploits orthogonal plasmonic slot waveguides while the second one exploits rotated plasmonic waveguides. For the orthogonal splitter, the transmission is more than -3.8 dB in port 1, when excited with a *y*-polarized polarization wave, and less than -14 dB in port 2. Moreover, the transmission results are exchanged when using an x-polarized wave. Similar results are also obtained for the rotated polarization splitter. The rotated splitter is able to guide the vertically propagating wave in a parallel horizontal plane. This provides horizontal propagation on different layers of a 3-D plasmonic circuit. These structures were simulated using 3-D FDTD utilizing both silver and aluminum. Our proposed devices may find various applications in integrated circuits that include logic gates, data multiplexing, filtering, and quadrature applications. Furthermore, they may aid in the realization of 3-D plasmonic chips for more compact and efficient processing.

Chapter 5

5.1 Conclusion

In conclusion, the limitations of electronics and the dielectric photonic components are illustrated. Then, we started of this thesis by an introduction to plasmonics and its unique characteristics, as well as the recent advances in this field. We mentioned a few designs that have the potential to play the interconnect role in ICs. Devices such as hybrid waveguides, PSWs, slit arrays, MIM and IMI couplers have been revealed and their configurations and applications discussed. The use of plasmonics is diverging to vast applications like sensing, focusing, imaging, solar cells, waveguiding, beam shaping and many more. The guiding of electromagnetic waves on a metal/dielectric interface proved to be a possible solution to various issues facing today's state of the art technology.

We then went on to portray an efficient technique for design optimization of plasmonic slit arrays. Through direct design of the phase profile, we reduce the number of optimizable parameters to only two. This vastly improved the optimization efficiency, and reduced its complexity. The technique accuracy is governed by the accuracy of the simulation and does not involve any approximations. After obtaining the optimal phase profile, a mapping is used to recover the actual physical parameters of the slit widths. We employ a multi-objective formulation to simultaneously optimize the focal length and the beam width resulting from the slit array. Our approach is effectively illustrated through a number of examples. Still, if the metal thickness was considered as an optimization parameter, it will increase the complexity due to the phase being affected by the metal thickness. Furthermore, considering different materials for the slit (instead of air), can lead to different characteristics regarding focusing and sensitivity. Moreover, more effective optimization techniques for plasmonic structures should be investigated. This will produce structures with high efficiency, taking into consideration the limitations of technology.

Furthermore, we presented two novel SPP polarization splitters utilizing the orthogonal junction coupling technique. This technique utilizes the wave vector match between the Si nano-wire and the PSWs. This coupling technique eliminates the need for tapering. The first structure proposed, exploits orthogonal plasmonic slot waveguides while the second one exploits rotated plasmonic waveguides, for horizontal manipulation. The first structure causes the incident beam to be split into two polarizations. One polarization is guided horizontally, while the other polarization is guided vertically. The device produces high transmissions with good splitting. The latter structure helps in rotating the vertically guided wave to a horizontal plane. The rotated wave is used for optical processing on different parallel layers, and thus realizing 3-D plasmonic chips. 3-D plasmonic chips increase the efficiency and the simultaneous processing of components on a circuit. The proposed structures possess wideband coupling and natural phase-matched Si nano-wire and plasmonic sections. These structures were simulated using 3-D FDTD utilizing both silver and aluminum. Our proposed devices may find various applications in integrated circuits that include logic gates, data multiplexing, filtering, and quadrature applications. The remaining challenge is to fabricate these devices with minimum fabrication deficiencies. Also, proposing different polarization rotators for the vertical PSW is essential to abet in realizing multi-layered plasmonic chips.

It is not a shock to see plasmonics dominate the technology industry in the years to come. With major advances happening in the field, SPPs are spreading like wild fire. Proper optimization of plasmonic devices is a must to realize more efficient systems. Moreover, developments in the fabrication techniques and recipes are needed to aid in better realization and reproducibility of these devices. More research into plasmonic 3-D circuits is required as this will vastly improve the efficiency and the processing capability of the systems.

References

[1] E. Ozbay, “Plasmonics: Merging Photonics and Electronics at the Nanoscale Dimensions,” Science, **311**, 189-193 (2006).

[2] M. J. Kobrinsky *et al*, “On Chip Optical Interconnects,” Intel Techno. J. **8**, 129-142 (2004).

[3] R. Zia, J. A. Schuller, A. Chandran, and M. L. Brongersma, “Plasmonics: the next chip-scale technology,” Mater. Today **9**, 20-27 (2006).

[4] A. Pratt, “Overview of the use of copper interconnects in the semiconductor industry," Tech. rep., Advanced Energy Industries, Inc., 2004.

[5] A. Biberman, and K. Bergman, “Optical interconnection networks for high-performance computing systems,” Rep. Prog. Phys. **75**, 046402 (2012).

[6] W. M. Green, M. J. Rooks, L. Sekaric, and Y. A. Vlasov, "Ultra-compact, low RF power, 10 Gb/s silicon Mach-Zehnder modulator," Opt. Express **15**, 17106-17113 (2007)

[7] D. K. Gramotnev, and S. I. Bozhevolnyi, “Plasmonics beyond the diffraction limit,” Nat. Photon. **4**, 83-91 (2010).

[8] W. L. Barnes, A. Dereux, and T. W. Ebbesen, “Surface plasmon subwavelength optics,” Nat. **424**, 824-830 (2003).

[9] D. Taillaert, P. Bienstman, and R. Baets, "Compact efficient broadband grating coupler for silicon-on-insulator waveguides," Opt. Lett. **29**, 2749-2751 (2004)

[10] F. Xia, M. Rooks, L. Sekaric, and Y. Vlasov, "Ultra-compact high order ring resonator filters using submicron silicon photonic wires for on-chip optical interconnects," Opt. Express **15**, 11934-11941 (2007)

[11] Y. Morita, Y. Tsuji, and K. Hirayama, “Proposal for a Compact Resonant-Coupling-Type Polarization Splitter Based on Photonic Crystal Waveguide with Absolute Photonic Bandgap,” IEEE Photon. Technol. Lett. **20**, 93-95 (2008).

[12] W. Bogaerts, R. Baets, P. Dumon, V. Wiaux, S. Beckx, D. Taillaert, B. Luyssaert, J. V. Campenhout,P. Bienstman, and D. V. Thourhout, “Nanophotonic Waveguides in Silicon-on-Insulator Fabricated With CMOS Technology,” J. Light. Technol **23**, 401-412 (2005)

[13] S. A. Maier, “Plasmonics: The Promise of Highly Integrated Optical Devices,” IEEE J. Sel. Quantum Electron. **12**, 1671-1677 (2006).

[14] J. Takahara, S. Yamagishi, H. Taki, A. Morimoto, and T. Kobayashi, "Guiding of a one-dimensional optical beam with nanometer diameter," Opt. Lett. **22**, 475-477 (1997)

[15] I. Choi, and Y. Choi, "Plasmonic Nanosensors: Review and Prospect," IEEE J. Sel. Quantum Electron. **PP**, 1-12 (2011).

[16] H. A. Atwater, and A. Polman, "Plasmonics for improved photovoltaic devices," Nat. Materials **9**, 205-213 (2010).

[17] S. A. Maier, *Plasmonics: Fundamentals and Applications* (Springer, New York, 2007), Chap. 2.

[18] P. B. Johnson, and R. W. Christy, "Optical constants of the noble metals," Phys. Rev. B **6**(12), 4370–4379 (1972).

[19] R. Zia, M. D. Selker, P. B. Catrysse, and M. L. Brongersma, "Geometries and materials for subwavelength surface plasmon modes," J. Opt. Soc. Am. **21**, 2442-2446 (2004)

[20] X. Guo, M. Qiu, J. Bao, B. J. Wiley, Q. Yang, X. Zhang, Y. Ma, H. Yu, and L. Tong, "Direct Coupling of Plasmonic and Photonic Nanowires for Hybrid Nanophotonic Components and Circuits," Nano Letts. **9**, 4515-4519 (2009).

[21] S. Lai, S. Link, and N. J. Halas, "Nano-optics from sensing to waveguiding," Nat. Photon. **1**, 641-648 (2007).

[22] G. Veronis, and S. Fan, "Theoretical investigation of compact couplers between dielectric slab waveguides and two-dimensional metal-insulator-metal plasmonic waveguide," Opt. Express **15**, 1211-1221 (2007).

[23] S. Zhu, T. Y. Liow, G. Q. Lo, and D. L. Kwong, “Silicon-based horizontal nanoplasmonic slot waveguides for on-chip Integration,” Opt. Express **19**, 8888-8902 (2011).

[24] B. Lau, M. A. Swillam, and A. S. Helmy, "Hybrid orthogonal junctions: wideband plasmonic slot-silicon waveguide couplers," Opt. Express **18**, 27048-27059 (2010).

[25] G. Veronis, and S. Fan, “Modes of Subwavelength Plasmonic Slot Waveguides,” J. Light. Technol. **25**, 2511-2521 (2007).

[26] R. A. Wahsheh, Z. Lu, and M. A. G. Abushagur, “Nanoplasmonic couplers and splitters,” Opt. Express **17**, 19033-19040 (2009).

[27] S. Sederberg, V. Van, and A. Y. Elezzabi, “Monolithic integration of plasmonic waveguides into a complimentary metal-oxide-semiconductor and photonic-compatible platform,” Appl. Phys. Lett. **96**, 121101 (2010).

[28] J. Mertz, “Radiative absorption, fluorescence, and scattering of a classical dipole near a lossless interface: a unified description,” J. Opt. Soc. Am. B **17**, 1906-1913 (2000).

[29] G. Xu, M. Tazawa, P. Jin, S. Nakao, and K. Yoshimura, “Wavelength tuning of surface plasmon resonance using dielectric layers on silver island films,” Appl. Phys. Lett. **82**, 3811-3813 (2003).

[30] H. Mertens, J. Veroeven, A. Polman, and F. D. Tichelaar, “Infrared surface plasmons in two-dimensional silver nanoparticle arrays in silicon,” Appl. Phys. Lett. **85**, 1317-1319 (2004).

[31] B. P. Rand, P. Peumans, and S. R. Forrest, “Long-range absorption enhancement in organic tandem thin-film solar cells containing silver nanoclusters,” J. Appl. Phys. **96**, 75197526 (2004).

[32] S. S. Kim, S. I- Na, J. Jo, D. Y. Kim, and Y.-C Nah, “Plasmon enhanced performance of organic solar cells using electrodeposited Ag nanoparticles,” Appl. Phys. Lett. **93**, 073307 (2008).

[33] V. E. Ferry, L. A. Sweatlock, D. Pacifici, and H. A. Atwater, “Plasmonic nanostructure design for efficient light coupling into solar cells,” Nano Lett. **8**, 4391-4397 (2008).

[34] F. J. Haug, T. Soderstrom, O. Cubero, V. Terrazzoni-Daudrix, and C. Ballif, “Plasmonic absorption in textured silver black reflectors of thin film solar cells,” J. Appl. Phys. **104**, 064509 (2008).

[35] C. Rockstuhl, S. Fahr, and F. Lederer, “Absorption enhancement in solar cells by localized plasmon polaritons,” J. Appl. Phys. **104**, 123102 (2008).

[36] M. A. Green, J. Zhao, A. Wang, S. R. Wenham, “Very high efficiency silicon solar cells: science and technology,” IEEE Trans. Electr. Dev. **46**, 1940-1947 (1999).

[37] J. Homola, "Surface plasmon resonance sensors for detection of chemical and biological species," Chem. Rev. **108**, 462-493 (2008).

[38] K. A. Willets, and R. P. Van Duyne, "Localized surface plasmon resonance spectroscopy and sensing," Ann. Rev. Physical Chem. **58**, 267-297 (2007).

[39] L. Moon, *et al.*, "In situ sensing of metal ion absorption to a thiolated surface using surface plasmon resonance spectroscopy," J. Colloid Interface Science **298**, 543-549 (2006).

[40] T. Kang, *et al.*, "Mesoporous silica thin films as a spatially extended probe of interfacial electric fields for amplified signal transduction in surface plasmon resonance spectroscopy," Chem. Comm., 2998-3000 (2006).

[41] T. Kang, *et al.*, "Reversible pH-driven conformational switching of tethered superoxide dismutase with gold nanoparticle enhanced surface plasmon resonance spectroscopy," J. Am. Chem. Soc. **128**, 12870-12878 (2006).

[42] A. G. Brolo, *et al.*, "Surface plasmon sensor based on the enhanced light transmission through arrays of nanoholes in gold films," Langumir **20**, 4813-4815 (2004).

[43] N. Irit, *et al.*, “Silica stabilized gold island films for transmission localized surface plasmon sensing,” J. Am. Chem. Soc. **129**, 84-92 (2007).

[44] A. J. Haes, *et al.*, “A localized surface plasmon resonance biosensor: first steps toward an assay for Alzheimer’s disease,” Nano Lett. **4**, 1029-1034 (2004).

[45] J. Zhao, *et al.*, “Resonance surface plasmon spectroscopy: Low molecular weight substrate binding to cytochrome P450,” J. Am. Chem. Soc. **128**, 11004-11005 (2006).

[46] C. Sonnichsen, *et al.*, “ A molecular ruler based on plasmon coupling of single gold and silver nanoparticles,” Nat. Biotech. **23**, 741-745 (2005).

[47] Y. W. Jun, *et al.*, “Continuous imaging of plasmon rulers in live cells reveals early-stage caspase-3 activation at the single molecule level,” Proceeding of the National Academy of Sciences of the United States of America **106**, 17735-17740 (2009).

[48] A. Grbic, and G. V. Eleftheriades, “Overcoming the Diffraction Limit with Planar Left-Handed Transmission-Line Lens,” Phys. Rev. Lett. **92**, 117403 (2004).

[49] Y. Fu, and X. Zhou, “Plasmonic Lenses: A Review,” Plasmonics **5**, 287-310 (2010).

[50] Z. Liu, S. Durant, H. Lee, Y. Pikus, N. Fang, Y. Xiong, C. Sun, and X. Zhan, “Far-Field Optical Superlens,” Nano Lett. **7**, 403-408 (2007).

[51] H. Lee, Z. Liu, Y. Xiong, C. Sun, and X. Zhang, "Development of optical hyperlens for imaging below the diffraction limit," Opt. Express **15**, 15886-15891 (2007).

[52] H. Shi, C. Du, and X. Luo, “Focal length modulation based on metallic slit surrounded with grooves in curved depths,” Appl. Phys. Lett **91**, 093111 (2007).

[53] H. Shi, C. Wang, C. Du, X. Luo, X. Dong, and H. Gao, "Beam manipulating by metallic nano-slits with variant widths," Opt. Express **13**, 6815-6820 (2005).

[54] L. Verslegers, P. B. Catrysse, Z. Yu, J. S. White, E. S. Barnard, M. L. Brongersma, and S. Fan, “Planar lenses based on nanoscale slit arrays in a metallic film,” *Nano Lett*., vol. 9, 2009, pp. 235–238.

[55] L.-B. Yu, D.-Z. Lin, Y.-C. Chen, Y.-C. Chang, K.-T. Huang, J.-W. Liaw, J.-T. Yeh, J.-M. Liu, C.-S. Yeh, and C.-K. Lee, “Physical origin of directional beaming emitted from a subwavelength slit,” Phys. Rev. B. **71**, 041405 (2005).

[56] Y. Fu, W. Zhou, and L. E. N. Lim, "Near-field behavior of zone-plate-like plasmonic nanostructures," J. Opt. Soc. Am. A **25**, 238-249 (2008).

[57] G. M. Lerman, A. Yanai, and U. Levy, “Demonstration of Nanofocusing by the use of Plasmonic Lens Illuminated with Radially Polarized Light,” Nano Lett. **9**, 2139-2143 (2009).

[58] D. Choi, Y. Lim, S. Roh, I.-M. Lee, J. Jung, and B. Lee, "Optical beam focusing with a metal slit array arranged along a semicircular surface and its optimization with a genetic algorithm," Appl. Opt. **49**, A30-A35 (2010).

[59] C. Forestiere, M. Donelli, G. F. Walsh, E. Zeni, G. Miano, and L. Dal Negro, "Particle-swarm optimization of broadband nanoplasmonic arrays," Opt. Lett. **35**, 133-135 (2010).

[60] C. Christopoulos, “The Transmission-Line Modeling Method: TLM,” Wiley-IEEE Press, 1995.

[61] FDTD Solutions, Lumerical Solutions, Inc., http://www.lumerical.com.

[62] Stephen Boyd & Lieven Vandenberghe, Convex Optimization, New York: Cambridge University Press, 2004, ch. 11.

[63] O. S. Ahmed, M. A. Swillam, M. H. Bakr, and Xun Li, "Modeling and design of nano-plasmonic structures using transmission line modeling," Opt. Express **18,** 21784-21797 (2010).

[64] S. A. Maier, M. L. Brongersma, P.G. Kik, S. Meltzer, A. A. G. Requicha, and H. A. Atwater, “Plasmonics- A Route to Nanoscale Optical Devices,” Advanced Materials **13,** 1501-1505 (2001).

[65] M. Raburn, B. Liu, K. Rauscher, Y. Okuno, N. Dagli, and J. E. Bowers, “3-D Photonic Circuit Technology,” IEEE J. Sel. Toics Quantum Electron. **8**, 935-942 (2002).

[66] S. N. Garner, S. Lee, V. Chuyanov, A. Chen, A. Yacoubian, W. H. Steier, and L. R. Dalton, “Three-Dimensional Integrated Optics Using Polymers,” IEEE J. Quantum Electron. **35**, 1146-1155 (1999).

[67] S. Nolte, M. Will, J.Burghoff, and A. Tuennermann, “Femtosecond waveguide writing: a new avenue to three-dimensional intergrated optics,” Appl. Phys. **A77**, 109-111 (2003).

[68] C. J. Brooks, A. P. Knights, and P. E. Jessop, “Vertically-integrated multimode interferometer coupler for 3D photonics circuits in SOI,” Opt. Express **19**, 2916-2921 (2011).

[69] Y. A. Vlasov, M. O’Boyle, H. F. Hamann, and S. J. McNab, “Active control of slow light on a chip with photonic crystal waveguides,” Nature **438**, 65-69 (2005).

[70] T. Barwicz, M. R. Watts, M. A. Popović, P. T. Rakich, L. Socci, F. X. Kärtner, E. P. Ippen, and H. I. Smith, “Polarization-transparent

microphotonic devices in the strong confinement limit," Nat. Photon. 1, 57-60 (2007).

[71] Y. Morita, Y. Tsuji, and K. Hirayama, "Proposal for a Compact Resonant-Coupling-Type Polarization Splitter Based on Photonic Crystal Waveguide with Absolute Photonic Bandgap," IEEE Photon. Technol. Lett. **20**, 93-95 (2008).

[72] H. Fukuda, K. Yamada, T. Tsuchizawa, T. Watanabe, H. Shinojima, and S. Itabashi, "Ultrasmall Polarization splitter based on silicon wire waveguides," Opt. Express **14**, 12401-12408 (2006).

[73] H. S. Won, K. C. Kim, S. H. Song, C. Oh, P. S. Kim et al, "Vertical coupling of long-range surface plasmon polaritons," Appl. Phys. Lett. **88**, 011110 (2006).

[74] C. Y. Tai, S. H. Chang, and T. Chiu, "Numerical optimization of wide-angle, broadband operational polarization beam splitter based on aniostropically coupled surface-plasmon-polariton wave," J. Opt. Soc. Am. A **25**, 1387-1392 (2008).

[75] C. L. Zou, F. W. Sun, C. H. Dong, X. F. Ren, J. M. Cui, X. D. Chen, Z. F. Han, and G. C. Guo, "Broadband integrated polarization beam splitter with surface plasmon," Opt. Lett. **36**, 3630-3632 (2011).

[76] N. Kiesel, C. Schmid, U. Weber, R. Ursin, and H. Weinfurter, “Linear Optics Controlled-Phase Gate Made Simple,” Phys. Rev. Lett. **95**, 210505 (2005).

[77] T. Yamazaki, J. Yamauchi, and H. Nakano, “A Branch-Type TE/TM Wave Splitter Using a Light-Guiding Metal Line,” IEEE J. Light. Technol., **25**, 922-928 (2007).

[78] J. Zhang, S. Zhu, H. Zhang, S. Chen, G. Lo, and D. Kwong, “An Ultra-Compact Polarization Rotator Based on Surface Plasmon Polariton Effect,” IEEE Photon. Technol. Lett. **23**, 1606-1608 (2011).

[79] M. Alam, J. S. Aitchsion, and M. Mojahedi, “Compact hybrid TM-pass polarizer for silicon-on-insulator platform,” Appl. Opt. **50**, 2294-2298 (2011)

[80] Y. F. Xiao, X. M. Lin, J. Gao, Y. Yang, Z. F. Han, and G. C. Guo, “Realizing quantum controlled phase flip through cavity QED,” Phys. Rev. A 70, 042314 (2004).

[81] H. Wei, Z. Wang, X. Tian, M. Käll, and H. Xu, “Cascaded logic gates in nanophotonic plasmon networks,” Nat. Comm. **2**, 1-5 (2011).

[82] E. D. Palik, *Handbook of optical constants of solids*, (Acadameic press, 1998).

[83] D. F. P. Pile and D. K. Gramotnev, “Plasmonic subwavelength waveguides: next to zero lossess at sharp bends,” Opt. Express **30**, 1186-1188 (2005).